JOURNAL OF GEOPHYSICAL RESEARCH, VOL. 114, C11023, doi:10.1029/2008JC005132, 2009

Click Here for Full Article

Probabilistic tsunami hazard assessment at Seaside, Oregon, for near- and far-field seismic sources

F. I. González,[1] E. L. Geist,[2] B. Jaffe,[3] U. Kânoğlu,[4] H. Mofjeld,[5] C. E. Synolakis,[6] V. V. Titov,[7] D. Arcas,[8] D. Bellomo,[9] D. Carlton,[10] T. Horning,[11] J. Johnson,[12] J. Newman,[8] T. Parsons,[2] R. Peters,[13] C. Peterson,[14] G. Priest,[15] A. Venturato,[16] J. Weber,[9] F. Wong,[2] and A. Yalciner[17]

Received 23 September 2008; revised 29 June 2009; accepted 17 July 2009; published 24 November 2009.

[1] The first probabilistic tsunami flooding maps have been developed. The methodology, called probabilistic tsunami hazard assessment (PTHA), integrates tsunami inundation modeling with methods of probabilistic seismic hazard assessment (PSHA). Application of the methodology to Seaside, Oregon, has yielded estimates of the spatial distribution of 100- and 500-year maximum tsunami amplitudes, i.e., amplitudes with 1% and 0.2% annual probability of exceedance. The 100-year tsunami is generated most frequently by far-field sources in the Alaska-Aleutian Subduction Zone and is characterized by maximum amplitudes that do not exceed 4 m, with an inland extent of less than 500 m. In contrast, the 500-year tsunami is dominated by local sources in the Cascadia Subduction Zone and is characterized by maximum amplitudes in excess of 10 m and an inland extent of more than 1 km. The primary sources of uncertainty in these results include those associated with interevent time estimates, modeling of background sea level, and accounting for temporal changes in bathymetry and topography. Nonetheless, PTHA represents an important contribution to tsunami hazard assessment techniques; viewed in the broader context of risk analysis, PTHA provides a method for quantifying estimates of the likelihood and severity of the tsunami hazard, which can then be combined with vulnerability and exposure to yield estimates of tsunami risk.

Citation: González, F. I., et al. (2009), Probabilistic tsunami hazard assessment at Seaside, Oregon, for near- and far-field seismic sources, *J. Geophys. Res.*, *114*, C11023, doi:10.1029/2008JC005132.

1. Background and Introduction

[2] There are multiple levels of tsunami hazard assessment (THA), including studies to investigate and document the frequency and severity of prehistoric and historic tsunami events, and numerical modeling studies with varying degrees of complexity, including worst case scenario simulations and sensitivity analyses to different sources. This paper describes probabilistic tsunami hazard assessment (PTHA), a method that provides the next level of predictability for the likelihood and severity of an event, and its application to Seaside, Oregon.

[3] Risk analysis provides the broader conceptual context for PTHA. Thus the term hazard is generally understood to deal only with the physical aspects of the phenomena and, in particular, the ability of the phenomena to inflict harm. Risk, on the other hand, although defined in many ways, invariably invokes probabilistic concepts. The World Meteorological Organization [*WMO*, 2008] adopts the widely accepted definition of *Crichton* [1999], based on his "risk triangle" concept: "Risk is the probability of a loss, and this depends on three elements: hazard, vulnerability, and exposure. If any of these three elements in risk

[1]Department of Earth and Space Sciences, University of Washington, Seattle, Washington, USA.
[2]U.S. Geological Survey, Western Coastal and Marine Geology, Menlo Park, California, USA.
[3]U.S. Geological Survey, Western Coastal and Marine Geology, Pacific Science Center, Santa Cruz, California, USA.
[4]Department of Engineering Sciences, Middle East Technical University, Ankara, Turkey.
[5]School of Oceanography, University of Washington, Seattle, Washington, USA.
[6]Viterbi School of Engineering, University of Southern California, Los Angeles, California, USA.
[7]NOAA Pacific Marine Environmental Laboratory, Seattle, Washington, USA.
[8]Joint Institute for the Study of Atmosphere and Ocean, University of Washington, Seattle, Washington, USA.
[9]Department of Homeland Security, FEMA, Washington, D.C., USA.
[10]ESA Adolfson, Seattle, Washington, USA.
[11]Horning Geoscience, Seaside, Oregon, USA.
[12]Northwest Hydraulics Consultants, Seattle, Washington, USA.
[13]Robert Peters Geologic, Davenport, California, USA.
[14]Department of Geology, Portland State University, Portland, Oregon, USA.
[15]Oregon Department of Geology and Mineral Industries, Coastal Field Office, Newport, Oregon, USA.
[16]Pierce County GIS Division, Tacoma, Washington, USA.
[17]Department of Civil Engineering, Middle East Technical University, Ankara, Turkey.

Copyright 2009 by the American Geophysical Union.
0148-0227/09/2008JC005132$09.00

increases or decreases, then the risk increases or decreases respectively." As with risk, multiple definitions of the terms vulnerability and exposure can be found in the relevant literature [*Thywissen*, 2006]. The United Nations Development Programme [*UNDP*, 2004] defines vulnerability as "A human condition or process resulting from physical, social, economic and environmental factors, which determine the likelihood and scale of damage from the impact of a given hazard" and exposure as "Elements at risk, an inventory of those people or artifacts that are exposed to a hazard."

[4] The corresponding general equation "Risk = function (Hazard × Vulnerability × Exposure)" [*WMO*, 2008] is one in which at least one of the three factors are probabilistic in nature, and with which most other definitions of risk are consistent. An example most relevant to this study is the working definition adopted by the U.S. National Tsunami Hazard Mitigation Program (NTHMP) [*Oppenheimer et al.*, 2009], i.e., "... risk is defined as the product of the probability of the occurrence of a tsunami (i.e., the "hazard") times the loss of property and life due to the tsunami." PTHA, then, provides a methodology for quantifying probabilities that characterize the hazard factor in risk analysis.

[5] Paleoearthquake, paleotsunami and historic studies indicate that Seaside has been struck by tsunamis generated by the seafloor displacement caused by local and distant earthquakes, i.e., near- and far-field tsunamis, respectively [*Fiedorowicz and Peterson*, 2002]. Every 500 years, on average, a great earthquake occurs on the Cascadia Subduction Zone (CSZ), almost certainly generating a very large near-field tsunami [*Petersen et al.*, 2008]; the most recent occurred in 1700. Three tsunamis of distant origin have caused notable flooding in Seaside: from Alaska in 1946, Chile in 1960, and Alaska in 1964 [*Lander et al.*, 1993] (http://www.ngdc.noaa.gov/hazard/tsu.shtml). The 1946 and 1960 wave amplitudes at Seaside were 1.2 and 1.5 m, respectively, and the 1964 flooding in Seaside reached heights of 5 m, caused one death, and destroyed 12 houses.

[6] Worst case scenario THA, in the form of community- and event-specific inundation modeling, has been employed since 1997 by State and Federal partners of the U.S. NTHMP to develop maps as planning tools for emergency management [*González et al.*, 2005]. Typically, these maps are developed through simulations of one or more scientifically defensible "credible worst case scenario(s)" involving local and/or distant earthquake sources. Earlier maps displayed only maximum inundation lines, but later versions now include tsunami time series at selected locations, maximum current speed estimates and, when available, paleotsunami and other relevant information [*Walsh et al.*, 2000; *Priest et al.*, 2009]. These maps represent essential scientific guidance for the development of practical emergency management products such as response plans and community-specific evacuation maps that define evacuation zones, pedestrian and vehicle evacuation routes, and safe assembly areas.

[7] Sensitivity analyses, also known as response analyses, can provide additional insight into the tsunami threat by exploiting a community-specific inundation model to simulate a suite of scenarios that identify the relative threat posed by different sources to different community locations. As an example, *Tang et al.* [2006] conducted a sensitivity study to assess the threat of tsunami inundation at Ford Island, Hawaii, the proposed site of a new National Oceanic and Atmospheric Administration (NOAA) facility; this analysis of nine historical and eighteen test tsunamis generated by seismic sources in all major Pacific Rim subduction zones concluded that tsunamis generated in the Kamchatka Subduction Zone posed the greatest potential threat to the study site. Sensitivity studies do not, however, address the probability of each scenario.

[8] PTHA provides estimates of the likelihood that tsunami flooding at a particular location will exceed a given level within a certain period of time. Development of this methodology and its application to Seaside, Oregon was conducted as a pilot project that was part of a U.S. Federal Emergency Management Agency (FEMA) initiative to modernize and upgrade Flood Insurance Rate Maps (FIRMs). For additional details, we refer the reader to the final report of the Tsunami Pilot Study Working Group [*TPSWG*, 2006].

2. Methodology

[9] PTHA integrates advanced tsunami inundation modeling with the analysis and statistical techniques developed in the field of probabilistic seismic hazard assessment (PSHA). In particular, the work of *Houston and Garcia* [1974, 1978], although groundbreaking for its time, was severely limited because it used a numerical model that did not include inundation computations, employed coarse grids of low-quality bathymetry and topography, considered only idealized far-field seismic source models, did not address near-field sources, and applied a probabilistic methodology based only on short-term historical tsunami records. In contrast, the PTHA methodology presented here utilizes inundation models run on high-quality bathymetric/topographic computational grids and initialized by crustal deformation models of near- and far-field earthquake sources, and uses source recurrence rate estimates based on both long-term paleoseismic and short-term historical tsunami records; the resulting database of inundation simulations is combined with predicted tide levels and subjected to a statistical analysis that provides recurrence rate estimates for tsunami amplitudes that exceed given values.

[10] Tsunami numerical simulations for this study were based on the method of splitting tsunami (MOST) model; the model hydrodynamics and numerical implementation are described by *Titov* [1997], *Titov and Synolakis* [1995, 1996, 1997, 1998] and *Titov and González* [1997]. Testing of the MOST model has been extensive, including comparisons with analytic and laboratory experiments, as described by *Synolakis et al.* [2008]. A number of successful case studies have also been documented, including the 1946 Alaska, 1992 Nicaragua, 1995 Mexico, 1994 Kuril, 1996 Peru, 1993 Okushiri, and the 2004 Indian Ocean tsunamis [*Yeh et al.*, 1995; *Titov and Synolakis*, 1996, 1997, 1998; *Titov*, 1997; *Titov and González*, 1997; *Bourgeois et al.*, 1999; *Titov et al.*, 2005; *Geist et al.*, 2006; *Arcas and Titov*, 2006; *Tang et al.*, 2008a, 2008b]. The performance and reliability of this model have led NOAA to select the

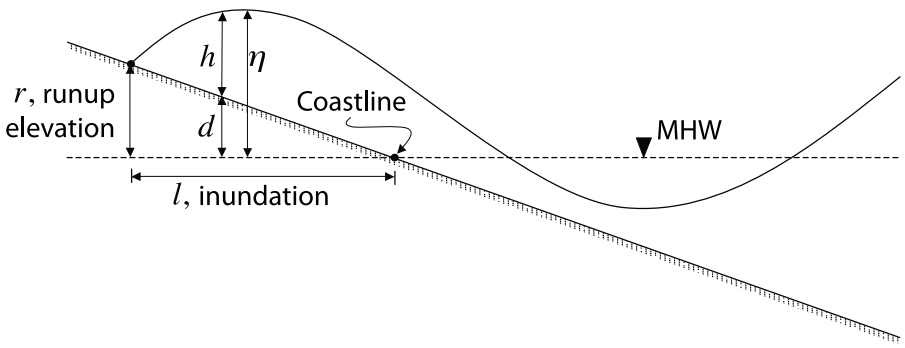

Figure 1. Definition sketch for MOST model variables. Not shown are (u, v), the depth-averaged current velocity components.

MOST model for operational real-time tsunami propagation and inundation forecasting [*Tang et al.*, 2008a; *Wei et al.*, 2008; *Titov*, 2009].

[11] PSHA was originally developed by *Cornell* [1968] and described in several reports, including that of the Senior Seismic Hazard Analysis Committee [*SSHAC*, 1997]. *Lin and Tung* [1982], *Rikitake and Aida* [1988], and *Downes and Stirling* [2001] modified PSHA to develop a PTHA that calculates wave heights using a simple source specification. In a related effort, a recent Puerto Rico Sea Grant report Natural Disaster Research [*NDR*, 2001] used both cumulative runup-frequency and rank-order statistics [*Sornette et al.*, 1996] derived from hydrodynamic modeling for calculating wave heights along the coast of Aguadilla, Puerto Rico. *NDR* [2001] included 1% annual probabilities of exceedance as well as a specification of the 10% probability of exceedance in 50 years.

[12] *Geist and Parsons* [2005] recently expanded these efforts by comparing empirical analyses of tsunami probabilities with computational PTHA. For a site such as Seaside that lacks an extensive historic record of tsunamis, computational PTHA provides a valuable tool for assessing tsunami risk. For the Cascadia region, *Geist and Parsons* [2005] compared PTHA results using end-member models of earthquake magnitude distributions: characteristic and Gutenberg-Richter (G-R). The latter involves a Monte Carlo simulation where the rupture location and slip distribution are randomized in the process of building a tsunami hazard curve (tsunami amplitude versus probability). They also compared an empirical estimate of far-field probabilities with the computational PTHA estimates for local tsunamis and later devised a Bayesian method to combine the computational and empirical approaches [*Parsons and Geist*, 2009]. For this study, tsunamis from a characteristic M $\sim$ 9 Cascadia earthquakes are used for the Seaside PTHA.

[13] The PTHA methods described in these previous studies are expanded here to develop, for the first time, a probabilistic tsunami flooding map. In this case, rather than calculating a hazard curve for a point on the coastline, a high-resolution grid is developed for the region around Seaside and a hazard curve is computed for each grid cell. For each grid cell hazard curve, the exceedance wave heights for the 1% and 0.2% annual probabilities are interpolated and the results mapped using Geographic Information System (GIS) software.

2.1. Inundation Computations

[14] The MOST code for inundation simulations are based on the nonlinear shallow-water wave equations

$$h_t + (uh)_x + (vh)_y = 0$$

$$u_t + uu_x + vu_y + gh_x = gd_x$$

$$v_t + uv_x + vv_y + gh_y = gd_y$$

where subscripts denote partial differentiation with respect to the Cartesian coordinates (x, y) and time, t, and where (see Figure 1)

h(x, y, t) = η(x, y, t) + d(x, y, t) is the flow depth,
η(x, y, t) is the wave amplitude,
d(x, y) is the undisturbed bathymetry and topography (measured positive down),
u(x, y, t) is the x-component of depth averaged current velocity,
v(x, y, t) is the y-component of depth averaged current velocity, and
g is the acceleration due to gravity.

Propagation computations are based on similar equations, but in a spherical coordinate system with Coriolis force included.

2.1.1. Computational Grids

[15] The Seaside-specific implementation of the MOST code, i.e., the "Seaside model," required the development of three imbedded grids: a Pacific Northwest region Grid A of relatively coarse ($\sim$1 km) resolution, a Washington-Oregon Grid B of intermediate ($\sim$180 m) resolution, and the finest resolution Seaside area Grid C. The resolution of Grid C was 30 m for local source scenarios, which were characterized by extensive inundation due to large waves that were relatively insensitive to smaller-scale coastal dunes; but Grid C resolution was 10 m for distant source scenarios, in order to better resolve coastal dune topography that could block smaller tsunami waves. This three-grid system was, in turn, imbedded in an existing Pacific-wide grid (Figure 2). The grids and the model output of wave amplitude and current velocity components were referenced to mean high water (MHW). Development of the Seaside grid system was a major and critical effort essential to this study, and App. B of *TPSWG* [2006] provides a detailed description of the data, procedures, methodologies and quality assurance.

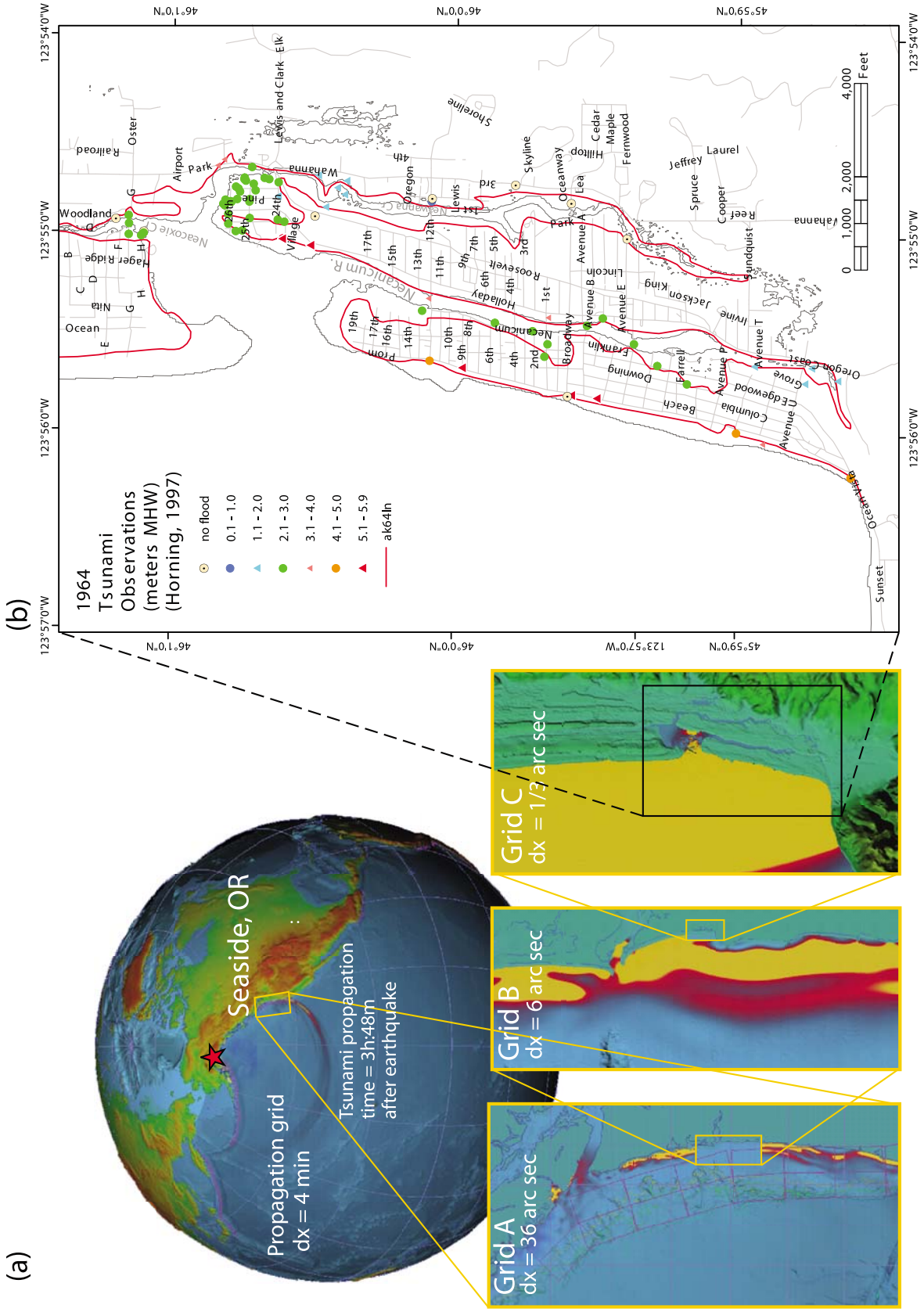

Figure 2. (a) The MOST model utilized three nested computational grids that telescoped down to the finest resolution Seaside area grid; initial and boundary conditions were provided at the perimeter of grid A by tsunami propagation solutions available in a precomputed database [*Titov et al.*, 2005]. A snapshot of the simulated 1964 Alaska tsunami is presented on the Pacific-wide grid as it nears Seaside and continues to propagate toward Hilo, Hawaii. (b) A summary of 1964 tsunami eyewitness observations [*TPSWG*, 2006, App. C] and a model-derived inundation line, ak64ln.

Table 1. Source Specification for Earthquakes Used in This Study[a]

Source	Location	M	Length (km)	Width (km)	Slip (m)	T_M (y)	Fault Model Specification[b]
1	AASZ	9.2	1000	100	17.7	1,313	A0–A9 and B0–B9 (Tsunami model 1 West)
2	AASZ	9.2	1000[c]	100	17.7[c]	750	A10–A19 and B10–B19 (Tsunami model 1 Mid)[c]
3	AASZ	9.2	600	100	Dist.	750	Distributed slip: 15 m * (A20 + B20) + 20 m * (A21 + B21) + 25 m * (A22 + B22) + 30 m * (A23 + B23 + A24 + B24 + A25 + B25) (Tsunami model 1 East)[c]
4	AASZ	9.2	1200	100	14.8[c]	1,133	A0–A11 and B0–B11 (Tsunami model 2 West)
5	AASZ	9.2	1200	100	14.8	750	A12–A23 and B12–B23 (Tsunami model 2 East)
6	AASZ	8.2	300	100	2.1	875	A17–A19 and B17–B19
7	AASZ	8.2	300	100	2.1	661	A20–A22 and B20–B22
8	AASZ	8.2	300	100	2.1	661	A23–A25 and B23–B25
9	KmSZ	8.8	500	100	9.8	100	A1–A5 and B1–B5
10	KmSZ	8.8	500	100	9.8	100	A6–A10 and B6–B10
11	KrSZ	8.5	300	100	5.8	500	A11–A13 and B11–B13
12	KrSZ	8.5	300	100	5.8	500	A14–A16 and B14–B16
13	KrSZ	8.5	300	100	5.8	500	A17–A19 and B17–B19
14	SChSZ	9.5	1100[c]	100	40.0	300	A35–A45 and B35–B45
15	CSZ	9.1	1100[c]	Variable	Variable	520	High-resolution model [*Flück et al.*, 1997]

[a]AASZ, Alaska-Aleutian Subduction Zone; KmSZ, Kamchatka Subduction Zone; KrSZ, Kuril Subduction Zone; SChSZ, Southern Chile Subduction Zone; CSZ, Cascadia Subduction Zone. T_M is the mean interevent time. Sources 1–14 are in the far-field and each letter/number entry in the Fault Model column refers to a single unit source of the NOAA/PMEL Facility for the Analysis and Comparison of Tsunami Simulations (FACTS), each characterized by uniform slip over a fault plane 100-km long and 50-km wide; multiple, adjacent FACTS unit sources are combined to form larger far-field sources, as noted. The near-field CSZ source was modeled with much finer resolution on a grid of 105 quadrilateral elements with varying dip and strike, and 12 different slip distributions were simulated to account probabilistically for this source of aleatory uncertainty (see text for discussion).

[b]FACTS unit sources numbering system has been changed since *TPSWG* [2006] was published; the old numbering system is used here.

[c]These values are corrections to typographical errors found in the corresponding table of *TPSWG* [2006].

2.1.2. Sources

[16] Here we provide only the briefest description of source specification; but, as in the case of the grid development effort, this was a fundamental and critical component of this study, and the reader is referred to *TPSWG* [2006] for detailed discussions of source specification in each subduction zone and the uncertainties associated with the process.

[17] Fifteen seismic sources in 5 active Pacific subduction zones were developed, consisting of the 14 far-field and 1 near-field events listed in Table 1, characterized by the earthquake magnitude (M) associated with the fault plane parameters and mean interevent times, T_M. Estimates of M for the Alaska-Aleutian and Cascadia Subduction Zones are essentially those specified in the National Seismic Hazard Maps [*Frankel et al.*, 1996, 2002; *Wesson et al.*, 1999, 2007; *Petersen et al.*, 2002, 2008]. Similarly, other published references were carefully reviewed to establish estimates for seismic parameters in the Kuril, Kamchatka and Chile Subduction Zones.

[18] Note that significantly reducing the number of required inundation simulations by specifying M-T_M pairs, rather than a range of earthquake magnitudes above a tsunamigenic threshold, is adequate for the goal of this study, because smaller earthquakes associated with a higher recurrence rate generate smaller tsunamis. Thus the inclusion of smaller, more frequent tsunamis in the probabilistic computations will have little impact on estimates of the 100- and 500-year exceedance wave amplitudes. Possible exceptions are smaller earthquakes in the Prince William Sound segment of the Alaska-Aleutian Subduction Zone that are optimally oriented for wave focusing at Seaside; to include this possibility, sources 6–8 were added, representing three adjacent, smaller magnitude earthquakes (M = 8.2), each with a different orientation that generates tsunamis with different directionality and therefore different focusing effectiveness at Seaside.

2.1.3. Initial and Boundary Conditions

[19] In all simulations, the initial sea surface displacement was assumed identical to the static seismic deformation of the earth's crust. Computational grids were adjusted to account for changes in bathymetry and topography due to this deformation, and dynamic boundary conditions were utilized at the common boundaries of all embedded grids. Far-field seismic deformation was modeled by the *Okada* [1985] fault plane solution with constant dip and slip over an area 100 km × 50 km; this coarse resolution was adequate because far-field inundation is sensitive primarily to earthquake magnitude and location but relatively insensitive to details of the deformation pattern [*Titov et al.*, 1999; *Okal and Synolakis*, 2008]. The corresponding tsunami propagation solutions were available in a precomputed database [*Titov et al.*, 2005], and these provided the initial and boundary conditions at Grid A. Near-field sources, however, required finer resolution modeling of crustal deformation, since near-field inundation is very sensitive to deformation pattern details. Initial conditions for the sea surface and the bathymetric/topographic computational grid were set by a fine-resolution crustal deformation model utilizing a grid of 105 quadrilateral elements with variable width, dip and slip [*Flück et al.*, 1997; *Priest et al.*, 1997; *Satake et al.*, 2003]; open ocean boundary conditions were applied on the perimeter of Grid A, which encompassed all near-field sources.

2.2. Probabilistic Computations

[20] Our goal is to establish, for multiple sources, the joint probability that flooding will exceed a particular value. We adopt an approach similar to that used by *Tetra Tech Inc.* [1981] to compute the combined probability of riverine and coastal flooding; a similar method was used by *Ward* [1994] to estimate the probability of ground shaking. Specifically, the method assumes that flood events can be described by a

Poisson distribution, which expresses the probability of a number of events occurring in a fixed period of time if these events occur with a known average rate and independently of the time since the last event. Thus if flooding level ζ exceeds a specific level ζ_i for each member of a set of multiple sources with known recurrence rates μ_j, then the Poissonian, time-independent probability that ζ_i will be exceeded due to the occurrence of the jth source during a period of time T is

$$P_{ij}(\zeta > \zeta_i) = 1 - \exp\left(-\mu_j T\right) \tag{1a}$$

and for all sources the combined probability that ζ_i will be exceeded is the product of the individual probabilities

$$\begin{aligned} P_i(\zeta > \zeta_i) &= 1 - \Pi_j\left(1 - P_{ij}\right) \\ &= 1 - \Pi_j \exp\left(-\mu_j T\right) = 1 - \exp(-\mu T) \end{aligned} \tag{1b}$$

so that the cumulative recurrence rate is seen to be the sum of the individual recurrence rates, i.e.,

$$\mu = \sum\nolimits_j \mu_j. \tag{1c}$$

[21] We adopt this Poissonian model in the work that follows. We also retain the i and j subscript convention used above to refer to exceedance levels and sources, respectively; i.e., in what follows, the i subscript is assigned to particular members of a set of specified flooding exceedance levels, ζ_i, and the j subscript is assigned to quantities associated with a particular member of the set of sources listed in Table 1.

2.2.1. Combined Exceedance Rates and Probabilities

[22] Here our specific goal is to calculate the 1% and 0.2% annual probabilities of exceedance for tsunami wave amplitude, taking into account of multiple tsunamigenic earthquake sources and multiple causes of uncertainty, such as the background tide level. The primary model output needed for this task is the maximum of the tsunami amplitude at each Seaside grid location, $\hat{\eta}$ (x, y), that occurs during each inundation simulation (or run) associated with each of the sources listed in Table 1; this basic data set of inundation runs is represented schematically in Figure 3a. These and other important ancillary data were incorporated by *Wong et al.* [2006] into a publicly accessible GIS database maintained by the U.S. Geological Survey; on completion of the study, all analysis results were also archived.

2.2.1.1. Tidal Stage, Including Aleatory Uncertainty

[23] Because the stage of the tide at tsunami arrival is unknown, this must be included in the probabilistic computations as a source of aleatory uncertainty. (Aleatory uncertainty is associated with the known, natural complexity of the physical process and cannot be reduced by additional data; in contrast, epistemic uncertainty is due to incomplete knowledge that can be reduced by additional data.) For this task, we use the method developed by *Mofjeld et al.* [1997, 2007], which improved on the approach utilized by *Houston and Garcia* [1978]. This theoretical and statistical study developed a convenient parametric expression for the probability density function (PDF) associated with the sum of the tides and a tsunami, in the form of a Gaussian distribution. To relate this work directly to our current study and notation conventions (Figure 1), we write the Gaussian approximation to the PDF function as

$$p[\zeta(x,y)|\hat{\eta}(x,y)] = \left[\sigma(2\pi)^{1/2}\right]^{-1} \exp\left\{-[\zeta(x,y) - \zeta_0]^2/2\sigma^2\right\}. \tag{2a}$$

Here the time series $\zeta(x, y, t) = \eta(x, y, t) + \xi(t)$ is the sum of the tsunami and tidal time series, η and ξ, respectively, and the parameters ζ_0 and σ are the mean height and standard deviation of the combined tsunamis and tide, respectively. However, note that temporal binning of values to form the PDF suppresses the time dependence of ζ in this and subsequent probabilistic equations; also, in the context of this analysis, the tides are considered to be locally independent of (x, y) and the (local) maximum amplitude of the incident tsunami, $\hat{\eta}$(x, y), is viewed as a parameter.

[24] As an alternative to the direct computation of ζ_0 and σ, empirical expressions as a function of $\hat{\eta}$ and standard tidal quantities were developed for each parameter

$$\begin{aligned} \zeta_0[\hat{\eta}(x,y)] &= \hat{\eta}(x,y) + MSL + C(MHHW - MSL) \\ &\quad \cdot \exp\left\{-\alpha[\hat{\eta}(x,y)/\sigma_0]^{\beta}\right\} \end{aligned} \tag{2b}$$

and

$$\sigma[\hat{\eta}(x,y)] = \sigma_0 - C'\sigma_0 \exp\left\{-\alpha'[\hat{\eta}(x,y)/\sigma_0]^{\beta'}\right\} \tag{2c}$$

where σ_0 is the standard deviation of the observed or predicted tides and MSL and MHHW are the values of mean sea level and mean higher high water, respectively; note that, in this formulation, MSL and MHHW are referenced to mean lower low water. Regression analysis then yields the 6 nondimensional parameters C, α, β, C′, α', and β'. To develop this result, *Mofjeld et al.* [1997, 2007] found that the statistics were adequately represented by employing a 5-day time series of a theoretical sinusoidal tsunami with a 20-minute wave period and maximum amplitude $\hat{\eta}$ that decreased exponentially with the 2.0-day decay constant that has been established for observed Pacific tsunamis. *Mofjeld et al.* [2007] provide details of the methodology and a table of these tidal and nondimensional parameters for 30 Pacific tide stations, including model-derived estimates for Seaside, Oregon.

2.2.1.2. Far-Field Sources, With Tidal Aleatory Uncertainty

[25] Inundation is relatively insensitive to the details of far-field slip distribution. Thus the far-field source models 1–14 in Table 1 are each in a discrete region, and each is associated with a single, specific set of earthquake parameters derived from fault plane elements of relatively coarse resolution (100 km × 50 km) [*TPSWG*, 2006, section 5.2.2]. In this sense, then, there is no uncertainty in the source parameters introduced into the probabilistic computations from far-field sources.

[26] To simplify the notation in what follows, we drop explicit reference to the spatial dependence of the variables ζ and η so that, for example, the jth far-field source in Table 1 is associated with a single inundation run that produces a single tsunami amplitude maximum, $\hat{\eta}_j$, at each grid position (x, y). Then the cumulative probability at each grid position that ζ will exceed a specific value ζ_i is given by the integral

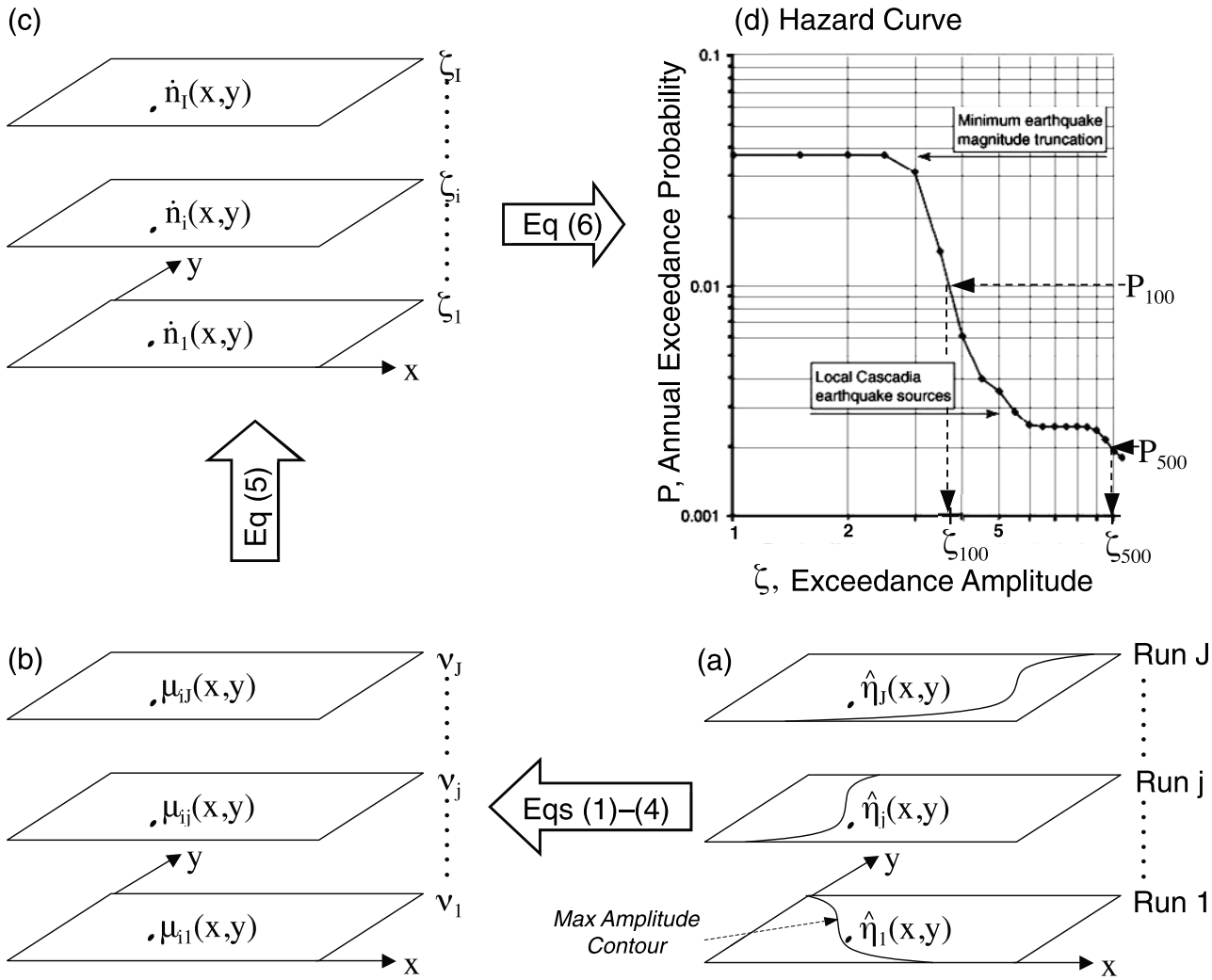

Figure 3. General procedure for developing probabilistic tsunami hazard map of exceedance wave amplitudes for the 0.01 and 0.002 a^{-1} recurrence rates. (a) Maximum tsunami amplitude is saved for each inundation simulation for a source in Table 1. (b) Combined exceedance rates are computed that account for three causes of flooding: earthquake occurrence, maximum tsunami amplitude, and the tides. (c) Cumulative exceedance rates for all sources in Table 1 and for specific exceedance values are formed by summing the combined rates in Figure 3b for each (x, y) position and specific exceedance value ζ_i. (d) Hazard curve for a representative location offshore Seaside, Oregon, identified in Figure 4. Each data point (ζ_i, P) is obtained by computing P from the cumulative exceedance rate in Figure 3c. Truncation of the hazard curve at high probability is caused by including only the largest earthquakes necessary for each subduction zone. Flattening of the hazard curve toward the tail is caused by using a characteristic earthquake model [cf., *Kagan*, 1996] for local Cascadia earthquake sources.

of the Gaussian PDF (equation (2a)) from ζ_i to ∞, which can be expressed in terms of the standard form of the error function, erf, as [see App. E, *TPSWG* [2006]]

$$P_{ij} = P_{ij}\left(\zeta > \zeta_i|\hat{\eta}_j\right) = \int_{\zeta_i}^{\infty} p\left(\zeta|\hat{\eta}_j\right)d\zeta$$
$$= \tfrac{1}{2}\left\{1 - \mathrm{erf}\left[\left(\zeta_i - \zeta_{0j}\right)/\left(2^{1/2}\sigma_j\right)\right]\right\} \quad (3a)$$

where the subscript j now appears on ζ_{0j} and σ_j to indicate their dependence on $\hat{\eta}_j$ through equation (2). We multiply this probability by the mean recurrence rate of each far-field source $\nu_j = 1/T_{M_j}$ (with T_M values provided in Table 1), to obtain the cumulative rate associated with the combined probability that the jth far-field earthquake and the associated maximum amplitude ζ_i will *both* occur

$$\mu_{ij} = \mu_{ij}\left(\zeta > \zeta_i|\hat{\eta}_j\right) = \nu_j P_{ij}$$
$$= \tfrac{1}{2}\nu_j\left\{1 - \mathrm{erf}\left[\left(\zeta_i - \zeta_{0j}\right)/\left(2^{1/2}\sigma_j\right)\right]\right\}. \quad (3b)$$

2.2.1.3. Near-Field Source, Including Tidal and Source Aleatory Uncertainty

[27] In contrast to sources in the far-field, details of the slip distribution for the near-field source have a strong effect on near-field inundation. Near-field slip distribution is

therefore a second source of aleatory uncertainty that must be taken into account. To deal probabilistically with this uncertainty, we created 12 fine resolution, near-field slip distributions in which the overall earthquake length was held constant, but the width and slip values were allowed to vary for 105 quadrilateral elements of the relatively fine resolution three-dimensional geometry model described by *Flück et al.* [1997] and *Satake et al.* [2003]. The moment magnitude associated with each of the slip distributions was held to the constant value listed in Table 1. These variations were subject to constraints imposed by the observed seismic source spectrum for subduction zone earthquakes [e.g., *Polet and Kanamori*, 2000] and, to establish that 12 slip distributions were adequate for the purposes of this study, the variation of peak nearshore tsunami amplitude was also modeled. Details of how we included slip distribution as a source of aleatory uncertainty for local CSZ earthquakes are provided in section 5.2.3.1 of *TPSWG* [2006].

[28] Thus the near-field CSZ source in Table 1 is associated with a *distribution* of maximum tsunami amplitude fields which, for the kth slip distribution, we write as $\hat{\eta}_{jk}(x, y)$, as distinguished from the single field of values $\hat{\eta}_j(x, y)$ associated with the jth discrete far-field source. The PDF for the kth slip distribution, including the effect of tides, is then given by the Gaussian distribution

$$p_k\left[\zeta(x,y)|\hat{\eta}_{jk}(x,y)\right] = \left[\sigma_{jk}(2\pi)^{1/2}\right]^{-1} \cdot \exp\left\{-\left[\zeta-\zeta_{0jk}\right]^2/2\sigma_{jk}^2\right\} \tag{4a}$$

and the probability that ζ will be greater than the exceedance value ζ_i for source j during the kth slip distribution is again the integral of this PDF from ζ_i to ∞

$$\begin{aligned} P_{ijk} = P_{ijk}\left(\zeta > \zeta_i|\hat{\eta}_{jk}\right) &= \int_{\zeta_i}^{\infty} p_k\left(\zeta|\hat{\eta}_{jk}\right)d\zeta \\ &= \left[\sigma_{jk}(2\pi)^{1/2}\right]^{-1}\int_{\zeta_i}^{\infty}\exp\left\{-\left[\zeta-\zeta_{0jk}\right]^2/2\sigma_{jk}^2\right\}d\zeta \\ &= {}^1\!/_2\left\{1-\mathrm{erf}\left[\left(\zeta_i-\zeta_{0jk}\right)/\left(2^{1/2}\sigma_{jk}\right)\right]\right\} \end{aligned} \tag{4b}$$

and for all slip distributions the combined probability that ζ_i will be exceeded is the product (see equation (1b)) over subscript k

$$\begin{aligned} P_{ij} = P_{ij}(\zeta > \zeta_i) &= 1 - \Pi_k\left(1 - P_{ijk}\right) \\ &= 1 - \Pi_k {}^1\!/_2\left\{1+\mathrm{erf}\left[\left(\zeta_i-\zeta_{0jk}\right)/\left(2^{1/2}\sigma_{jk}\right)\right]\right\}. \end{aligned} \tag{4c}$$

[29] As for far-field sources, this combined probability is now multiplied by the mean recurrence rate of the near-field source, which for the CSZ source is $\nu_j = 1/T_{M_j} = 1/520\ a^{-1}$, to obtain the cumulative rate associated with the combined probability that the near-field earthquake and the associated maximum amplitude ζ_i will both occur

$$\begin{aligned} \mu_{ij} = \mu_{ij}\left(\zeta > \zeta_i|\hat{\eta}_j\right) &= \nu_j P_{ij} \\ &= \nu_j\left[1 - \Pi_k {}^1\!/_2\left\{1+\mathrm{erf}\left[\left(\zeta_i-\zeta_{0jk}\right)/\left(2^{1/2}\sigma_{jk}\right)\right]\right\}\right]. \end{aligned} \tag{4d}$$

Note that this expression incorporates two sources of aleatory untertainty: tidal stage and slip distribution.

2.2.2. Cumulative Exceedance Rates and the 100- and 500-Year Exceedance Probabilities

[30] We now specify a discrete set of exceedance levels, say $\{\zeta_i\} = \{1.0, 1.5, 2.0, \ldots 10.5\}$, and perform the computations outlined in equations (1)–(4) to obtain GIS layers of the values μ_{ij} for each layer associated with the jth source and the source recurrence rate, ν_j (Figure 3b). For each specific value of ζ_i, the cumulative rate $\dot{n}$ at which ζ exceeds ζ_i is given by a summation over the source subscript j of the individual rates μ_{ij} for each individual source, i.e.,

$$\dot{n}_i(\zeta > \zeta_i) = \sum\nolimits_j \mu_{ij}(\zeta > \zeta_i) \tag{5}$$

where it is understood that computations for far-field sources, j = 1 to 14 in this study, and computations for near-field sources that include slip uncertainty, j = 15 in this study, are governed by equations (3) and (4), respectively. This summation is represented schematically as the GIS layers in Figure 3c, where now each layer is associated with a specific exceedance value, ζ_i.

[31] Then for all sources, the combined probability that ζ_i will be exceeded is given by

$$P_i(\zeta_i, T) = 1 - \exp(\dot{n}_i T) \tag{6}$$

and we obtain the annual probability of exceedance by setting T = 1 year. (Annual probability and cumulative rates are often used interchangeably, because equation (6) is approximately $\dot{n}_i$ for small $\dot{n}_i T$.) Thus equations (5) and (6) yield a set of (exceedance level, annual probability) pairs $[\zeta_i, P_i(x, y)]$ that constitute data points of a hazard curve that can be constructed at every position (x, y). Figure 3d presents an example of a hazard curve, illustrating how ζ_{100} and ζ_{500} values can be obtained graphically at each position (x, y) to produce the final GIS layers, $\zeta_{100}(x, y)$ and $\zeta_{500}(x, y)$.

[32] Finally, a regression analysis is used to obtain a parametric equation $P = f(\zeta)$ and/or the inverse equation $\zeta = g(P)$ at each position (x, y) that, when solved individually for P equal to 0.01 and 0.002 a^{-1}, yields the annual probabilities associated with the maximum amplitude exceedance levels for the 100- and 500-year tsunamis, $\zeta_{100}(x, y)$ and $\zeta_{500}(x, y)$, respectively. Figure 4 presents the contour maps of the maximum amplitude fields $\zeta_{100}(x, y)$ and $\zeta_{500}(x, y)$, i.e., the 100- and 500-year tsunami maps that correspond to 0.01 and 0.002 annual probabilities of exceedance, respectively. Note that only the mathematics of the process have been outlined here, not the implementation; the creation of these layers from actual study data was considerably more complicated due to practical issues such as spatial data resolution, appropriate smoothing, and accurate interpolation. For details of the GIS procedures utilized for this task, see *Wong et al.* [2006] and App. G of *TPSWG* [2006].

3. Field Data

[33] Tsunami flooding often leaves behind distinctive sheets of sand that can be interpreted to estimate the age, frequency, severity, and spatial distribution of the minimum

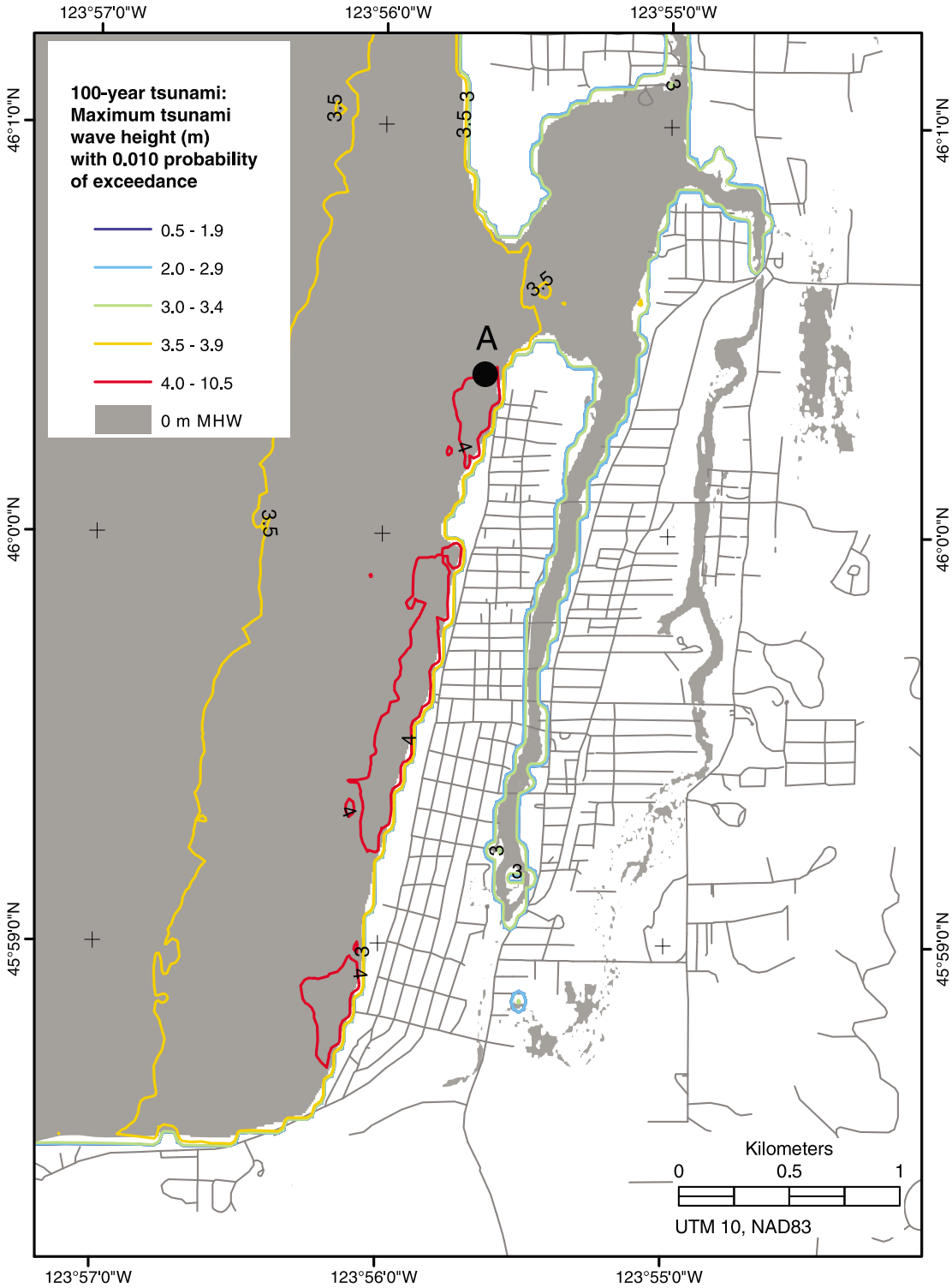

Figure 4a. Maximum tsunami wave amplitudes (m) with a 1% annual probability of exceedance. Wave amplitudes include the effects of tides. Contours are color coded over the indicated range. Point A is the location of the hazard curve presented in Figure 3 and the disaggregation analyses in Figure 5. The 0 m MHW level was derived from aerial photos acquired in 2000 [*TPSWG*, 2006, App. B]. Contour lines are labeled with lowest value of the range indicated in the legend. Some low amplitude contours may be hidden by high amplitude contours in regions of high amplitude gradients.

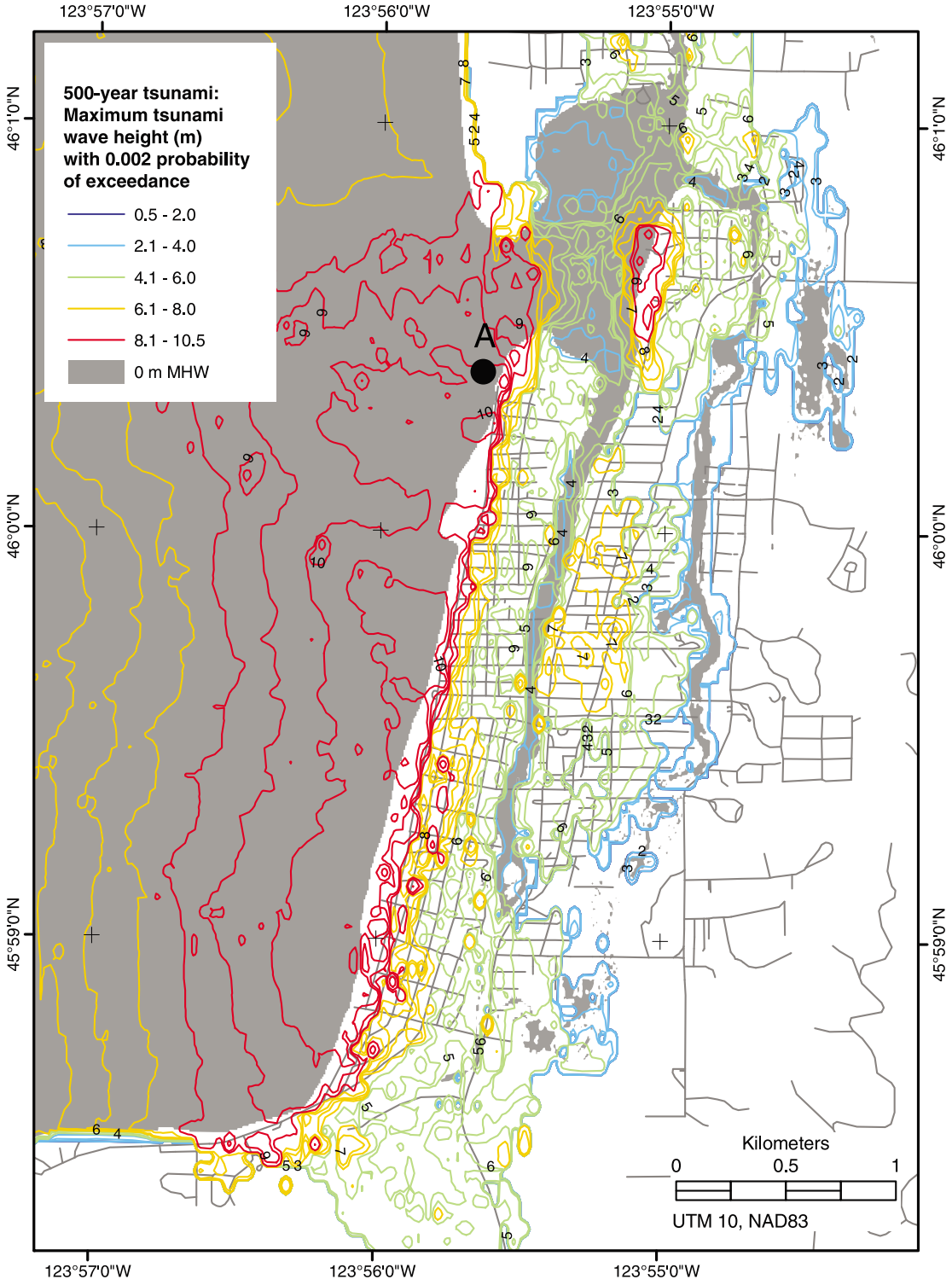

Figure 4b. Maximum tsunami wave amplitudes (m) with a 0.2% annual probability of exceedance. Wave amplitudes include the effects of tides. Contours are color coded over the indicated range. Point A is the location of the hazard curve presented in Figure 3 and the disaggregation analyses in Figure 5. The 0 m MHW level was derived from aerial photos acquired in 2000 [*TPSWG*, 2006, App. B]. Contour lines are labeled with lowest value of the range indicated in the legend. Some low amplitude contours may be hidden by high amplitude contours in regions of high amplitude gradients.

extent of tsunami inundation [*Jaffe and Gelfenbaum*, 2002; *Dawson and Stewart*, 2007; *Bourgeois*, 2008]. Such sandy evidence for past tsunamis has been found at Seaside in cores, trenches, and the banks of tidal streams [*Fiedorowicz*, 1997; *Fiedorowicz and Peterson*, 2002]. We found additional evidence at another 76 sites [*TPSWG*, 2006, App. D]. Deposits formed by five tsunamis in the past 2000 years were found at 167 sites located as far as 2 km inland along 5 km of Seaside coast. Deposits were primarily found in marshes fringing the Necanicum River and Neawanna Creek, which flow parallel to the coast between beach ridges that are 5 to 10 m high. Geological and archeological evidence indicates that these and other high gravel ridges have been present at Seaside for many centuries [*Fiedorowicz*, 1997].

[34] Where there is a suitable environment for deposition and preservation of tsunami deposits, data from modern tsunamis indicate that the inland extent of tsunami deposits and flooding are usually within 50 m of one another [*Gelfenbaum and Jaffe*, 2003; *Jaffe et al.*, 2003]. However, it must be kept in mind that inundation extent based on deposits can be in error for a number of reasons; for example, a deposit may never have formed for lack of sediment sources, a storm deposit might be mistaken for a tsunami deposit, or a tsunami deposit may simply have eroded. Careful analysis and interpretation of deposit data is therefore crucial, and we refer the reader to section 4 of *TPSWG* [2006] for a detailed discussion of the Seaside work, including the multiple criteria applied to judge the validity of the deposits. For comparison with the 100- and 500-year tsunami estimates, we focused on defining inundation by the 1964 far-field and 1700 near-field tsunamis.

3.1. Far-Field 1964 Alaska Tsunami

[35] Tsunami deposits from the 1964 Alaskan tsunami were identified at 116 sites, typically within a few tens of centimeters of the surface, with features very different from those of a storm deposit [*Morton et al.*, 2007]. A database of 66 eyewitness observations of 1964 runup and water levels was also available that proved very useful in the search for additional deposits by helping identify other known sites of 1964 tsunami inundation [*Fiedorowicz*, 1997; Figure 2b; *TPSWG*, 2006, App. C]. Figure 6a presents the locations of tsunami deposits, eyewitness data and the 0.5–1.9 m exceedance amplitude contour for the 100-year tsunami.

[36] A MOST model simulation was also conducted, even though model accuracy was thought to be compromised by differences in bathymetry and topography that existed in 1964 and the computational grid developed for this study; DEM development in and around the Necanicum River mouth was biased toward data less than 10 years old, but the shoreline of the Seaside coast and Necanicum estuary are highly dynamic, and an analysis documented significant changes in this area over a 55-year period, due to accretion and erosion [*TPSWG*, 2006, App. B]. Nonetheless, with this caveat in mind, the model-derived inundation line is also overlain on Figure 6a, because it is broadly consistent with field observations with the exception of one notable feature: the modeled tsunami penetrates significantly farther up Neawanna Creek than indicated by eyewitness reports (see also Figure 2b).

3.2. Near-Field 1700 Cascadia Tsunami

[37] Deposits from the 1700 tsunami were present at 119 sites in the Seaside area up to 2 km inland (Figure 6b and App. D of *TPSWG* [2006]); these are usually found approximately 0.5–1 m below the surface and formed sand sheets in many areas that were laterally continuous for tens to hundreds of meters. Many areas possibly inundated by the 1700 tsunami could not be sampled because of residential and commercial development. Figure 6b presents a summary of the available field data overlain with the 0.5–2.0 m exceedance amplitude contour for the 500-year tsunami.

4. Discussion

4.1. Probabilistic Results

4.1.1. The 100- and 500-Year Tsunamis

[38] As seen in Figure 4, offshore values of both the 100- and 500-year tsunami maximum amplitude are amplified by shoaling as tsunamis propagate shoreward, reach a maximum value along the coastline, then generally decrease in value with distance inland as tsunamis lose energy through interactions with topography; a similar pattern can be seen along the estuary coastline, albeit with a generally lower level of values overall. One limitation on 100-year inundation extent and tsunami maximum amplitude is the existence of coastal dunes south of the estuary mouth that block most far-field tsunamis, but are easily overtopped by large, near-field tsunamis. An additional factor that reduces these 100-year tsunami estimates is that far-field sources that do cause significantly higher inundation are likely associated with mean interevent times substantially longer than 100 years. For example, we assumed a mean interevent time of 750 years for a source similar to the 1964 Alaska earthquake (Source 3, Table 1), and eyewitness reports indicate that the 1964 inundation significantly exceeded the 100-year maximum amplitude estimates, apparently approaching 6 m at some locations (Figure 2b). Thus while the 500-year map is dominated by very large tsunamis with maximum amplitudes in excess of 8 m along the entire Seaside coastline and inland penetration is in excess of 1 km, the 100-year map reflects the incidence of more frequent far-field tsunamis with typically smaller coastal maximum amplitudes of 3.5–4 m and more limited inundation that is essentially restricted to the estuarine coastline.

[39] To quantify source contributions to the Seaside tsunami hazard, we applied a disaggregation analysis [*McGuire*, 1995; *Bazzurro and Cornell*, 1999] to the probabilistic results at offshore Seaside Point A, for which the 100- and 500-year maximum tsunami amplitudes are 4 m and 10 m, respectively (Figure 4). The results presented in Figure 5 indicate that (a) 100-year tsunamis with maximum offshore amplitude of 4 m are generated primarily by sources in the Cascadia, Alaska-Aleutian, and southern Chile Subduction Zones (CSZ, AASZ, and SChSZ, respectively), with the AASZ the largest contributor to the hazard, and (b) not surprisingly, local Cascadia earthquakes dominate the generation of 500-year tsunamis with maximum offshore amplitude of 10 m.

[40] It is thus of interest to compare the 100- and 500-year maps with tsunami deposit data acquired for the far-field

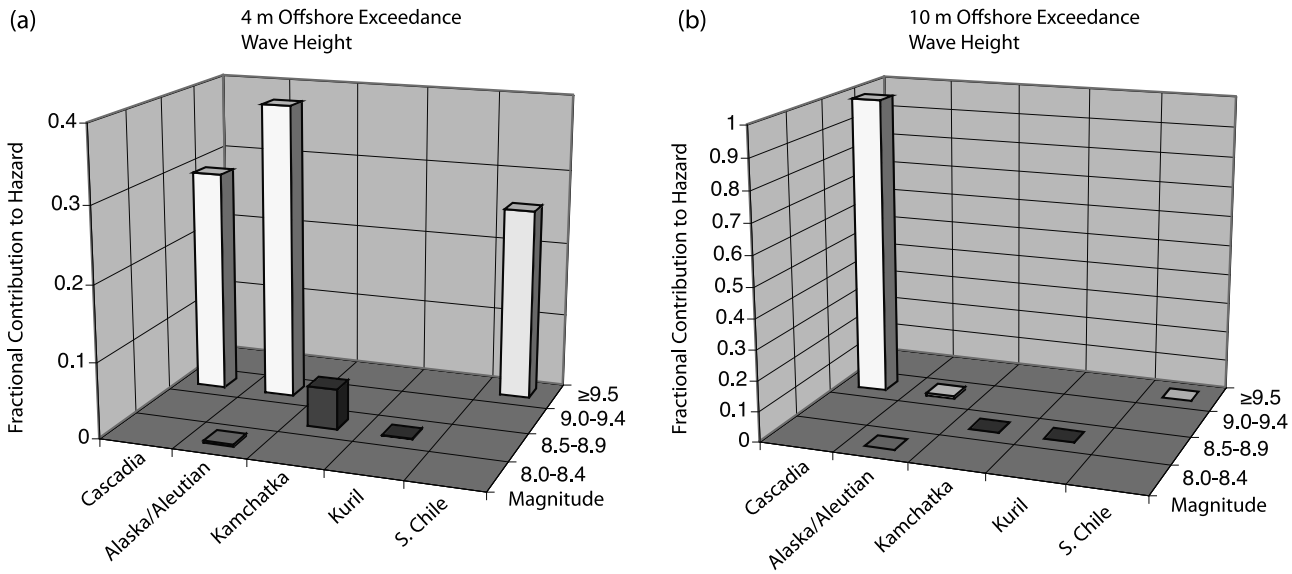

Figure 5. Disaggregation analysis of the relative contribution of source regions to the Seaside tsunami hazard, conducted for the offshore Point A indicated in Figures 4a and 4b [see *McGuire*, 1995; *Bazzurro and Cornell*, 1999]. (a) 100-year tsunamis with 4 m offshore waves. (b) 500-year tsunamis with 10 m offshore waves.

1964 Alaska and the near-field 1700 CSZ tsunamis, respectively, keeping in mind that there are limitations in the interpretation of tsunami deposits, because not all deposits are preserved. A commonly accepted view of tsunami deposits, however, is that they represent minimum estimates of inundation extent, primarily as a result of two mechanisms: first, a minimum, nonzero amplitude is assumed necessary for formation of deposits, so that a tsunami with amplitude less than this minimum might penetrate farther inland without deposition; second, erosion of deposits will also lead to an underestimate of deposit-based inundation extent values.

[41] The landward extent of the 1964 and 1700 tsunami deposits are about the same distance inland as that of the smallest amplitude contours for the 100- and 500-year tsunami maps, suggesting that preservation is not a significant issue at Seaside (Figure 6). Also note that some 1700 Cascadia tsunami deposits are found up to 2 km inland near the base of hills east of Seaside, indicating that the tsunami overtopped the ridge east of Neawanna Creek; thus the 1700 tsunami was large even at this great distance inland. In contrast, 1964 tsunami deposits are confined to the margins of Neawanna Creek and the Necanicum River, indicating a smaller tsunami that was not able to overtop the ridges.

[42] The presence of tsunami deposits far inland that are older than 1700 is evidence that the 1700 tsunami is not an outlier in terms of size and that the Seaside area has been inundated by large tsunamis in the past; thus although a large number of Seaside sites (312) have been examined for tsunami deposits, it is probable that further investigations will increase the estimate of the area of inundation, especially for older tsunamis.

4.1.2. Additional Sources of Uncertainty

[43] This work included a probabilistic treatment of the uncertainty in tide level at the time of tsunami arrival, and the uncertainty in details of the near-field Cascadia slip distribution. Here we briefly mention other sources of uncertainty in the probabilistic computations and, where possible, their effect on the results.

4.1.2.1. Inter-Event Time Estimates

[44] In Figure 3d, we show the hazard curve for a representative offshore location, Position A. The hazard curve deviates from a linear log-log relationship at high probability because of the decision to use a characteristic (M_{max}) earthquake [cf., *Kagan*, 1996]. If smaller earthquakes were included for both far-field and local sources, it is likely that the hazard curve would be more linear in log-log space [see *Geist and Parsons*, 2005]. Correspondingly, this part of the curve and the 0.2% annual exceedance probability estimate can be significantly affected by the uncertainty in the interevent time for this earthquake.

[45] *TPSWG* [2006] section 8.2 explores the effect of Cascadia mean interevent time uncertainty by developing 500-year maps based on Cascadia mean interevent times of 477 and 610 years, which are both within the range constrained by paleoseismic data [*Atwater et al.*, 2004]. Uncertainty related to empirical estimates of recurrence rate is quantified using Monte Carlo techniques [*Parsons*, 2008]. The shorter mean interevent time results in significant changes in the 500-year tsunami map, but increasing the mean interevent time to 610 years results in little change.

4.1.2.2. Background Sea Level

[46] All inundation modeling was conducted under the assumption that, to first order, interaction between tsunami and tides can be modeled by linear superposition. In addition, all inundation modeling was conducted by setting the background water level to a constant value of MHW. A statistical analysis to estimate the consequence of maintaining a constant MHW level results in a maximum upward bias of 0.2–0.7 m (7–10%) on the 100- and 500-year maximum tsunami amplitude exceedance values [section 2.5, *TPSWG*, 2006].

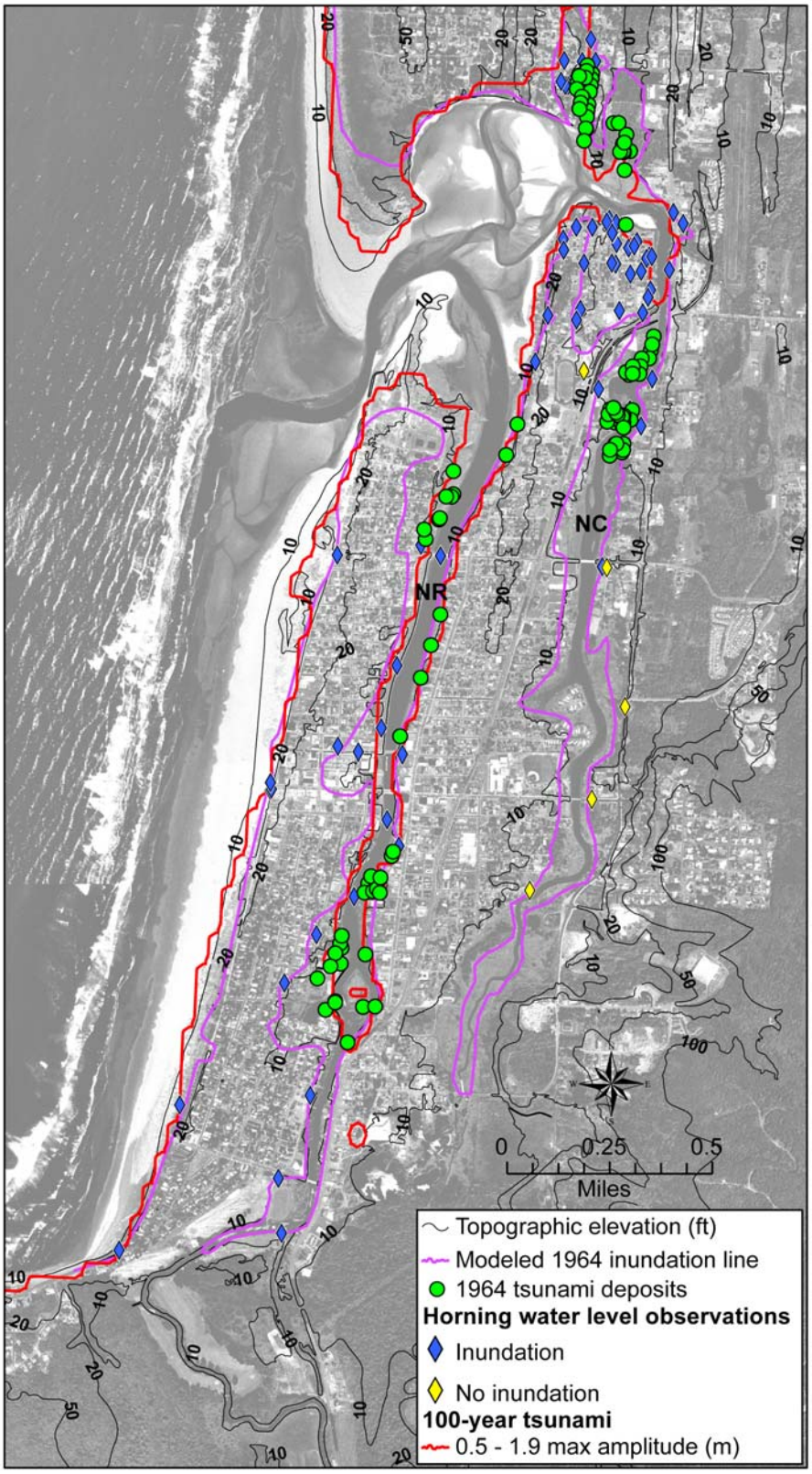

Figure 6a. Overview of 1964 tsunami data, including the location of deposits and water level observations, a model-derived inundation line, and the contour for the lowest range, and therefore the farthest inland penetration, of maximum amplitude for the 100-year tsunami. The Necanicum River and Neawanna Creek are annotated as NR and NC, respectively.

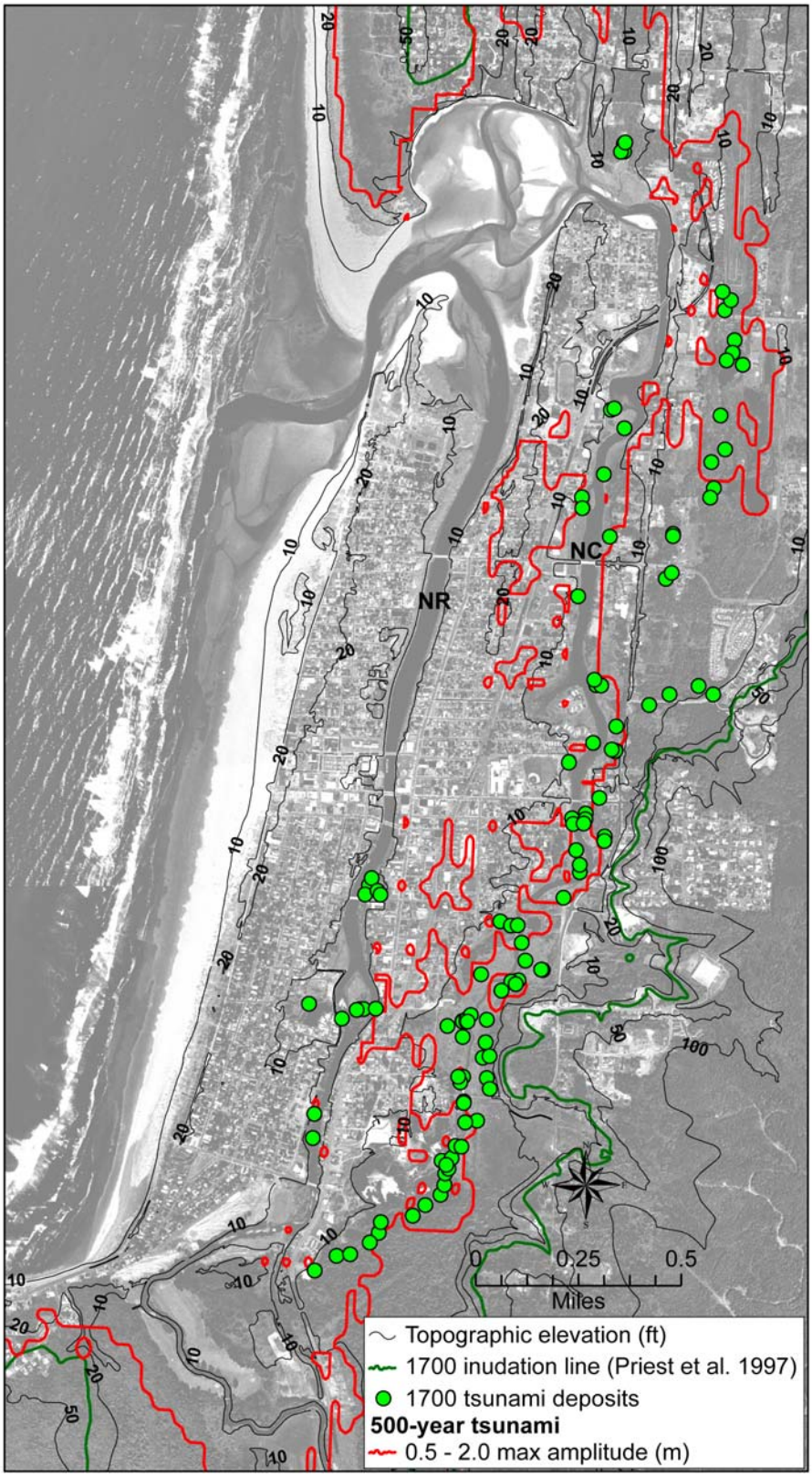

Figure 6b. Overview of 1700 tsunami data, including the location of deposits, an inundation line developed by *Priest et al.* [1997], and the contour for the lowest range, and therefore the farthest inland penetration, of maximum amplitude for the 500-year tsunami. The Necanicum River and Neawanna Creek are annotated as NR and NC, respectively.

4.1.2.3. Bathymetry and Topography

[47] *TPSWG* [2006] presents abundant evidence that the dynamic Seaside nearshore and estuarine environment is characterized by significant changes in bathymetry and topography on a timescale of decades. Thus the width of the Necanicum River mouth has varied between a minimum of 300 m and maximum of 800 m over 6–7 decades as a consequence of southern accretion and erosion in a cycle of about 15 years and northern accretion at a rate of approximately 7 m/a. Similarly, the outer coast north of the Necanicum River mouth displays a general trend of accretion averaging 3.2 m/a. More dramatically, Curt Peterson and David Percy (Portland State University) found a paleo-inlet approximately 1 to 1.5 km south of the current inlet by means of a preliminary investigation utilizing Ground Penetrating Radar.

[48] Inlet location is a primary control on Seaside tsunami inundation. The 1964 tsunami deposits, for example, extended farthest inland at the inlet, indicating that it served as a conduit for the tsunami; this effect has also been noted in historic tsunami observations [*Synolakis and Bernard*, 2006]. Shoreline position change is clearly another important factor governing tsunami inundation and subsequent estimates of the extent of this inundation. Thus the inland extent of inundation will be decreased/increased by shoreline accretion/erosion, and estimates based on tsunami deposits will overestimate/underestimate the inland extent of inundation if the shoreline has accreted/eroded since the tsunami occurred.

[49] It was beyond the scope of this study to construct multiple computational grids to deal with this uncertainty in a formal probabilistic way and/or test the sensitivity of our results to bathy/topo changes that have occurred in the past and may recur in the future; indeed, reliable bathy/topo data are not available for such an effort. Rather, we utilized an inundation model bathy/topo grid that was carefully developed from the best available bathymetric and topographic data; since, as a general rule, the best bathy/topo data are also the most recently acquired, the grid was biased toward modern Seaside bathymetric and topographic conditions.

4.2. Inundation Model Results

[50] We did not conduct a sensitivity study, such as that of *Tang et al.* [2006], of Seaside flooding sensitivity to the characteristics of the suite of sources in Table 1. However, we do present here one striking example of this sensitivity to the characteristics of two AASZ sources, and discuss the importance of currents in assessing tsunami hazard.

4.2.1. Flooding Sensitivity to Source Characteristics

[51] Subduction zone tsunamigenic earthquake sources can be quite linear along strike, and line sources tend to create a directional beam of concentrated energy [*Ben-Menahem and Rosenman*, 1972]. Figure 7a presents two beams generated by AASZ sources 3 and 5; the beams are made apparent by saving the maximum tsunami amplitude computed at each position during a simulation. Ignoring differences in the beams caused by propagation through somewhat different bathymetric regimes, we note that each source is characterized by the same total energy provided by a $M_w = 9.2$ earthquake but that they differ in length and position; Source 3 is 600 km shorter and is positioned 200 km farther northwest than Source 5. As a consequence, Source 3 energy density is higher, i.e., the beam is more intense, and the beam axis is farther north. This means that Source 3 focuses more energy on Seaside than Source 5, as is clear from Figure 7a, resulting in higher maximum amplitude and current speed values, as seen in Figures 7b and 7c.

[52] Local effects due to refraction, reflection, and scattering may also contribute to differences seen in the Seaside response to Sources 3 and 5, since these processes are a function of the incident wave angle. However, it is likely that far-field source characteristics dominate the response, since long tsunami waves tend to line up with the bathymetry traversed during propagation, thus reducing differences in the angle of incidence on the Northwest coast. Nonetheless, we note that we have not conducted a detailed analysis of the effect of important regional features resolved by the computational grid, including the Juan de Fuca Ridge, seamount chains farther offshore, the Astoria Canyon, and the bight between the Columbia River and Tillamook Head.

4.2.2. Current Speed Versus Wave Amplitude

[53] High currents do not necessarily correspond to high wave amplitude during tsunami flooding. For example, *Carrier et al.* [2003] and *Kânoğlu* [2004] investigated the case of simple plane beach geometry and found that the highest current speed does not occur coincidentally with the greatest wave amplitude and that the location of the region of highest speed depends on details of the incoming wave, and thus on the particular scenario under study. In fact, relatively modest wave amplitude can be accompanied by extremely high current speeds that cannot be neglected, because the associated kinetic energy can be the most destructive aspect of a tsunami [*Synolakis*, 2004]. In our study, this feature of tsunami flooding is demonstrated by Figures 7b and 7c, with the most dramatic example apparent in the river entrance and adjacent bay, where both Sources 3 and 5 produce relatively low wave amplitude, but very high current speed. This lack of correspondence between maximum wave amplitude and current speed means that maps of maximum wave height could be dangerously misleading, i.e., the overall tsunami hazard and destructive potential could be seriously underestimated in areas of modest wave height because destructively high currents were not taken into account in determining the exposure to tsunami hazards.

4.2.3. Impact Metrics

[54] Tsunami impact forces are far less understood than propagation and inundation; nonetheless, a more complete and appropriate hazard assessment would take account of both wave amplitude and currents, i.e., both potential and kinetic energy, by developing "impact indices" or "impact metrics." The FEMA Coastal Construction Manual formulations rely on riverine flooding results, with flow velocity and forces inferred through largely empirical relationships involving only the flow depth; but this is not adequate, because tsunami flow patterns can be more complex and counterintuitive, even for the fairly simple topography of a plane beach. As an alternative, computation and mapping of the following metrics would add significant value to any tsunami hazard assessment: flow depth, current speed, acceleration, inertia (flow depth $\times$ acceleration), and momentum flux (flow depth $\times$ square of current speed). A more detailed discussion of such metrics is provided in section 7 of *TPSWG* [2006] and, in the context of nuclear

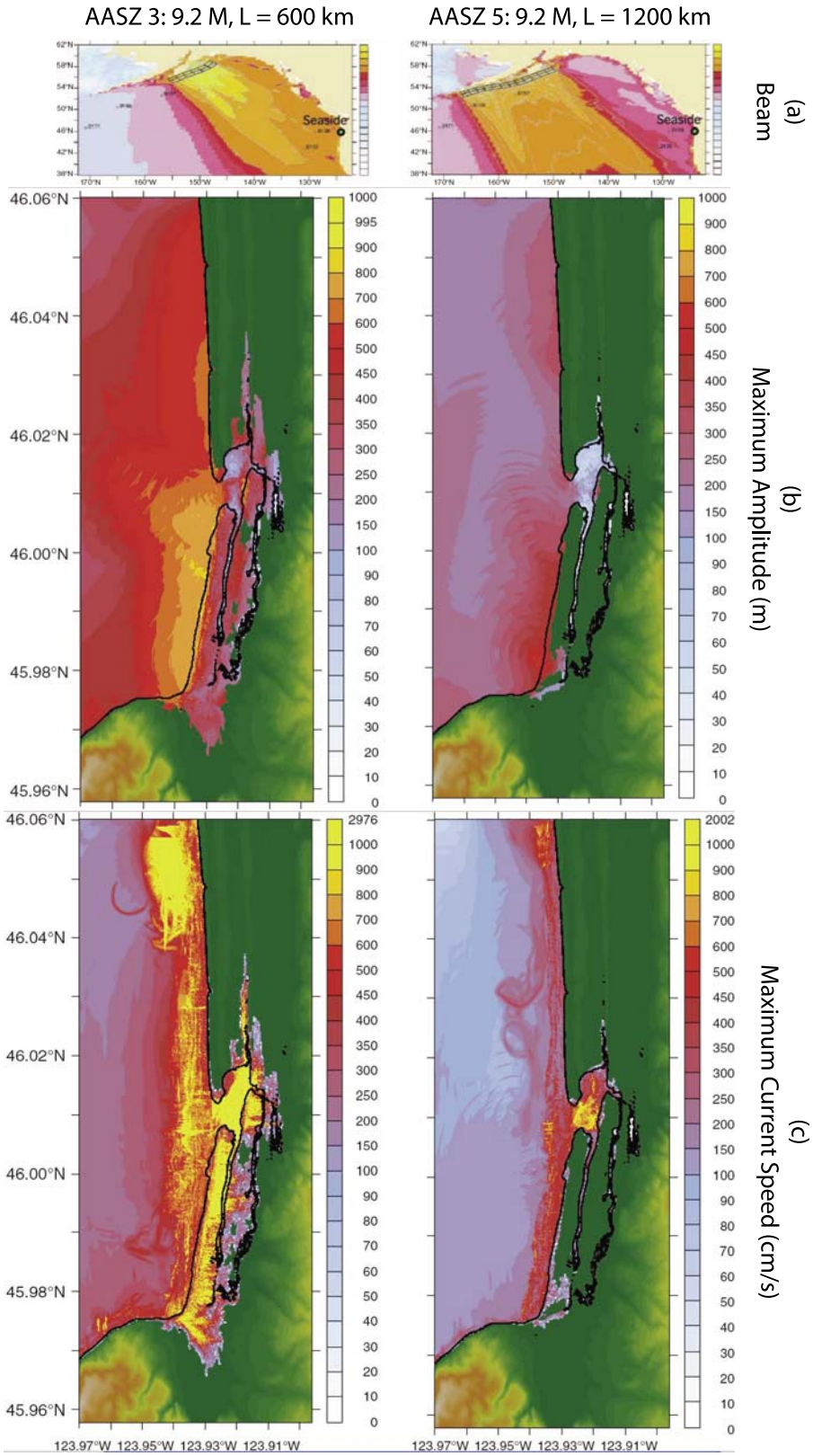

Figure 7. Sensitivity of Seaside maximum amplitude and current speed to source beam intensity and direction. (a) Tsunami beams for Sources 3 and 5, composed of the (100 km × 50 km) unit sources listed in Table 1, with label A indicating the most seaward row, and label numbers increasing to the east. (b) Maximum amplitude. (c) Maximum current speed.

power plant site assessments, in section 6 of *González et al.* [2007].

5. Summary and Conclusions

[55] We have applied a probabilistic tsunami hazard methodology to Seaside, Oregon that combines modern tsunami inundation modeling with probabilistic concepts and methods adapted from seismic hazard assessment. The methodology represents a major advance over previous methods and should therefore be applied to upgrade assessments in other coastal areas.

[56] PTHA methods can be significantly improved through focused research in both hydrodynamics and geophysics. Hydrodynamic research is needed to properly include nonlinear tide/tsunami interactions into inundation models, and a better understanding of the physics of forces on structures is needed to develop improved tsunami impact metrics. Research is also needed to more accurately date and constrain mean interevent times of paleoseismic events, and to better define prehistoric shorelines, topography, and bathymetry for improved interpretation of tsunami deposits. Collaborative hydrodynamic and geological research is needed to provide a better understanding of paleotsunami events, with a special focus on tsunami-induced erosion and deposition processes that create tsunami deposits and alter tsunami penetration into estuaries and coastal rivers; as an example, additional studies are needed to better define the Seaside paleoinlet and when it was open to the sea, coupled with inundation modeling that incorporates the paleoinlet feature. Similar collaborative research is needed to extend PTHA to include subaerial and subaqueous landslides as additional source mechanisms.

[57] **Acknowledgments.** We thank Brian Atwater and an anonymous reviewer for their thorough reviews and constructive comments. Similarly, we thank Frederic Raichlen and Robert Dean for their comprehensive reviews of the original Tsunami Pilot Study Working Group [*TPSWG*, 2006] report, which resulted in this paper. High-resolution fault geometry for the Cascadia interplate thrust was generously provided by Kelin Wang. This publication is partially funded by the Joint Institute for the Study of the Atmosphere and Ocean (JISAO) under NOAA Cooperative Agreement Number NA17RJ1232, contribution number 1596, PMEL contribution number 3240.

References

Arcas, D., and V. Titov (2006), Sumatra tsunami: Lessons from modeling, *Surv. Geophys.*, *27*, 679–705, doi:10.1007/s10712-006-9012-5.

Atwater, B. F., M. P. Tuttle, E. S. Schweig, C. M. Rubin, D. K. Yamaguchi, and E. Hemphill-Haley (2004), Earthquake recurrence inferred from paleoseismology, *Dev. Quat. Sci.*, *1*, 331–350.

Bazzurro, P., and C. A. Cornell (1999), Disaggregation of seismic hazard, *Bull. Seismol. Soc. Am.*, *89*, 501–520.

Ben-Menahem, A., and M. Rosenman (1972), Amplitude patterns of tsunami waves from submarine earthquakes, *J. Geophys. Res.*, *77*, 3097–3128.

Bourgeois, J. (2008), Chapter 3. Geologic Effects and Records of Tsunamis, in *The SEA, Volume 15: Tsunamis*, edited by A. R. Robinson and E. N. Bernard, pp. 53–91, Harvard Univ. Press, Cambridge, Mass.

Bourgeois, J., C. Petroff, H. Yeh, V. Titov, C. Synolakis, B. Benson, J. Kuroiwa, J. Lander, and E. Norabuena (1999), Geologic setting, field survey and modeling of the Chimbote, northern Peru, tsunami of 21 February 1996, *Pure Appl. Geophys.*, *154*(3/4), 513–540.

Carrier, G. F., T. T. Wu, and H. Yeh (2003), Tsunami runup and drawdown on a plane beach, *J. Fluid Mech.*, *475*, 79–99.

Cornell, C. A. (1968), Engineering seismic risk analysis, *Bull. Seismol. Soc. Am.*, *58*, 1583–1606.

Crichton, D. (1999), The risk triangle, in *Natural Disaster Management*, edited by J. Ingleton, pp. 102–103, Tudor Rose, London, U. K.

Dawson, A. G., and I. Stewart (2007), Tsunami deposits in the geological record, *Sediment. Geol.*, *200*, 166–183.

Downes, G. L., and M. W. Stirling (2001), Groundwork for development of a probabilistic tsunami hazard model for New Zealand, in *International Tsunami Symposium 2001*, edited by E. Bernard, pp. 293–301, Pacific Marine Environmental Lab., Seattle, Wash.

Fiedorowicz, B. K. (1997), Geologic evidence of historic and prehistoric tsunami inundation at Seaside, Oregon, M.S. Thesis, 197 pp., Portland State Univ., Portland, OR.

Fiedorowicz, B. K., and C. D. Peterson (2002), Tsunami deposit mapping at Seaside, Oregon, USA, in *Geoenvironmental Mapping: Methods, Theory, and Practice*, edited by P. T. Bobrowski, pp. 629–648, A. A. Balkema, Lisse, Netherlands.

Flück, P., R. D. Hyndman, and K. Wang (1997), Three-dimensional dislocation model for great earthquakes of the Cascadia subduction zone, *J. Geophys. Res.*, *102*, 20,539–20,550.

Frankel, A. D., C. S. Mueller, T. Barnhard, D. M. Perkins, E. V. Leyendecker, N. Dickman, S. Hanson, and M. Hopper (1996), National seismic-hazard maps, Documentation, *U.S. Geological Survey, Open-File Rep. 96-532*, 41 pp., June.

Frankel, A. D., et al. (2002), Documentation for the 2002 Update of the National Seismic Hazard Maps, *U.S. Geological Survey, Open-File Rep. 02-420*, 33 pp.

Geist, E. L., and T. Parsons (2005), Probabilistic analysis of tsunami hazards, *Nat. Hazards*, *37*(3), 277–314.

Geist, E. L., V. V. Titov, and C. E. Synolakis (2006), Wave of Change, pp. 56–65., *Sci. Am.*, Jan.

Gelfenbaum, G., and B. E. Jaffe (2003), Erosion and sedimentation from the 17 July 1998 Papua New Guinea tsunami, *Pure Appl. Geophys.*, *60*, 1969–1999.

González, F. I., et al. (2005), Progress in NTHMP hazard assessment, *Nat. Hazards*, *35*, 89–110.

González, F. I., et al. (2007), Scientific and technical issues in tsunami hazard assessment of nuclear power plant sites, *NOAA Tech. Memo. OAR PMEL-136*, NTIS: PB2008-101460, Pacific Marine Environmental Laboratory, Seattle, Wash., 125 pp. + appendices on CD.

Houston, J. R., and A. W. Garcia (1974), Type 16 Flood Insurance Study: Tsunami Predictions for Pacific Coastal Communities, U.S. Army Engineer Waterways Experiment Station, *Tech. Rep. H-74-3*.

Houston, J. R., and A. W. Garcia (1978), Type 16 Flood Insurance Study: Tsunami Predictions for the West Coast of the Continental United States, U.S. Army Engineer Waterways Experiment Station, *Tech. Rep. H-78-26*.

Jaffe, B. E., and G. Gelfenbaum (2002), Using tsunami deposits to improve assessment of tsunami risk, in *Solutions to Coastal Disasters '02*, edited by L. Ewing and L. Wallendorf, pp. 836–847, ASCE, Reston, Va.

Jaffe, B. E., G. Gelfenbaum, D. Rubin, R. Peters, R. Anima, M. Swensson, D. Olcese, L. Bernales, J. Gomez, and P. Riega (2003), Tsunami deposits: Identification and interpretation of tsunami deposits from the June 23, 2001 Peru tsunami, in *International Conference on Coastal Sediments 2003*, edited by R. A. Davis, A. Sallenger, and P. Howd, 13 pp., World Sci., Fl.

Kagan, Y. Y. (1996), Comment on "The Gutenberg-Richter or characteristic earthquake distribution, which is it?" by Steven G. Wesnousky, *Bull. Seismol. Soc. Am.*, *86*, 274–285.

Kânoğlu, U. (2004), Nonlinear evolution and runup-rundown of long waves over a sloping beach, *J. Fluid Mech.*, *513*, 363–372.

Lander, J. F., P. A. Lockridge, and M. J. Kozuch (1993), Tsunamis Affecting the West Coast of the United States 1806–1992, NGDC Key to Geophysical Record Documentation No. 29, NOAA, NESDIS, NGDC, 242 pp.

Lin, I., and C. C. Tung (1982), A preliminary investigation of tsunami hazard, *Bull. Seismol. Soc. Am.*, *72*, 2323–2337.

McGuire, R. K. (1995), Probabilistic seismic hazard analysis and design earthquakes: Closing the loop, *Bull. Seismol. Soc. Am.*, *85*, 1275–1284.

Mofjeld, H. O., M. G. G. Foreman, and A. Ruffman (1997), West coast tides during Cascadia Subduction Zone tsunamis, *Geophys. Res. Lett.*, *24*(17), 2215–2218.

Mofjeld, H. O., F. I. González, V. V. Titov, A. J. Venturato, and J. C. Newman (2007), Effects of tides on maximum tsunami wave heights: Probability distributions, *J. Atmos. Ocean. Technol.*, *24*(1), 117–123.

Morton, R., G. Gelfenbaum, and B. E. Jaffe (2007), Physical criteria for distinguishing sandy tsunami and storm deposits using modern examples, *J. Sediment. Geol.*, *200*(3–4), 184–207.

Natural Disaster Research (NDR) I. (2001), Probabilistic Tsunami Hazard Analysis: Aguadilla, Puerto Rico Sea Grant College Program, University of Puerto Rico, Project R-122-1-97, 28 pp.

Okada, Y. (1985), Surface deformation due to shear and tensile faults in a half-space, *Bull. Seismol. Soc. Am.*, *75*, 1135–1154.

Okal, E. A., and C. E. Synolakis (2008), Far-field tsunami risk from megathrust earthquakes in the Indian Ocean, *Geophys. J. Int.*, *172*(3), 995–1015.

Oppenheimer, D., J. Rhoades, M. Roberts, C. von Hillebrandt-Andrade, P. Whitmore, and C. Williams (2009), National Tsunami Hazard Mitigation Program 2009–2013 Strategic Plan, 34 pp., U.S. NTHMP, Silver Spring, Md. (Available at http://nthmp.tsunami.gov/)

Parsons, T. (2008), Monte Carlo method for determining earthquake recurrence parameters from short paleoseismic catalogs: Example calculations for California, *J. Geophys. Res.*, *113*, B03302, doi:10.1029/2007JB004998.

Parsons, T., and E. L. Geist (2009), Tsunami probability in the Caribbean region, *Pure Appl. Geophys.*, *165*, 1226–2089.

Petersen, M. D., C. H. Cramer, and A. D. Frankel (2002), Simulations of seismic hazard for the Pacific Northwest of the United States from earthquakes associated with the Cascadia subduction zone, *Pure Appl. Geophys.*, *159*, 2147–2168.

Petersen, M. D., et al. (2008), Documentation for the 2008 Update of the United States National Seismic Hazard Maps, *Open-File Rep. 2008–1128*, U.S. Department of the Interior, U.S. Geological Survey, 60 pp. and Appendices.

Polet, J., and H. Kanamori (2000), Shallow subduction zone earthquakes and their tsunamigenic potential, *Geophys. J. Int.*, *142*, 684–702.

Priest, G. R., E. Myers, A. M. Baptista, P. Fleuck, K. Wang, R. A. Kamphaus, and C. D. Peterson (1997), Cascadia subduction zone tsunamis: Hazard mapping at Yaquina Bay, Oregon, State of Oregon, Department of Geology and Mineral Industries, *Open-File Rep. O-97-34*, 144 pp.

Priest, G. R., C. Goldfinger, K. Wang, R. C. Witter, Y. Zhang, and A. M. Baptista (2009), Tsunami hazard assessment of the Northern Oregon coast: A multi-deterministic approach tested at Cannon Beach, Clatsop County, Oregon, Oregon Department of Geology and Mineral Industries Special Paper 41. (Available at http://www.naturenw.org/store-maps.htm)

Rikitake, T., and I. Aida (1988), Tsunami hazard probability in Japan, *Bull. Seismol. Soc. Am.*, *78*, 1268–1278.

Satake, K., K. Wang, and B. F. Atwater (2003), Fault slip and seismic moment of the 1700 Cascadia earthquake inferred from Japanese tsunami descriptions, *J. Geophys. Res.*, *108*(B11), 2535, doi:10.1029/2003JB002521.

Senior Seismic Hazard Analysis Committee (SSHAC) (1997), Recommendations for Probabilistic Seismic Hazard Analysis: Guidance on Uncertainty and Use of Experts, U.S. Nuclear Regulatory Commission, Main Rep. NUREG/CR-6372 UCRL-ID-122160 Vol. 1, 256 pp.

Sornette, D., L. Knopoff, Y. Y. Kagan, and C. Vanneste (1996), Rank-ordering statistic of extreme events: Application to the distribution of large earthquakes, *J. Geophys. Res.*, *101*, 13,883–13,893.

Synolakis, C. E. (2004), Tsunami and Seiche, in *Earthquake Engineering Handbook*, edited by W. F. Chen and C. Scawthorn, pp. 9-1–9-90, CRC Press, Washington, D. C.

Synolakis, C. E., and E. N. Bernard (2006), Tsunami science before and beyond Boxing Day 2004, *Philos. Trans. R. Soc. A*, *364*(1845), 2231–2265, doi:10.1098/rsta.20.

Synolakis, C. E., E. N. Bernard, V. V. Titov, U. Kânoğlu, and F. I. González (2008), Validation and verification of tsunami numerical models, *Pure Appl. Geophys.*, *165*(11–12), 2197–2228.

Tang, L., C. Chamberlin, E. Tolkova, M. Spillane, V. V. Titov, E. N. Bernard, and H. O. Mofjeld (2006), Assessment of potential tsunami impact for Pearl Harbor, Hawaii, *NOAA Tech. Memo. OAR PMEL-131*, NTIS: PB2007-100617, 36 pp.

Tang, L., C. Chamberlin, and V. V. Titov (2008a), Developing tsunami forecast inundation models for Hawaii: Procedures and testing, *NOAA Tech. Memo. OAR PMEL-141*, 46 pp.

Tang, L., V. V. Titov, Y. Wei, H. O. Mofjeld, M. Spillane, D. Arcas, E. N. Bernard, C. Chamberlin, E. Gica, and J. Newman (2008b), Tsunami forecast analysis for the May 2006 Tonga tsunami, *J. Geophys. Res.*, *113*, C12015, doi:10.1029/2008JC004922.

Tetra Tech Inc. (1981), Coastal Flooding Storm Surge Model, Federal Emergency Management Agency: Part 1. Methodology, Federal Emergency Management Agency, Washington, D. C.

Thywissen, K. (2006), Components of Risk: A Comparative Glossary, United Nations University, Institute of Environment and Human Security, 52 pp. (Available at www.ehs.unu.edu/file.php?id=118)

Titov, V. V. (1997), Numerical modeling of long wave runup, Ph.D. thesis, Univ. of Southern California, Los Angeles, Calif.

Titov, V. V. (2009), Tsunami Forecasting, in *The SEA, Volume 15: Tsunamis*, edited by E. N. Bernard and A. R. Robinson, pp. 371–400, Harvard Univ. Press.

Titov, V. V., and F. I. González (1997), Implementation and testing of the Method of Splitting Tsunami (MOST) model, *NOAA Technical Memorandum ERL PMEL-112*, 11 pp.

Titov, V. V., and C. E. Synolakis (1995), Modeling of breaking and nonbreaking long wave evolution and runup using VTCS-2, *J. Waterw. Port C-ASCE*, *121*(6), 308–316.

Titov, V. V., and C. E. Synolakis (1996), Numerical Modeling Of 3-D Long Wave Runup Using VTCS-3, in *Long Wave Runup Models*, pp. 242–248, World Sci., Singapore.

Titov, V. V., and C. E. Synolakis (1997), Extreme inundation flows during the Hokkaido-Nansei-Oki tsunami, *Geophys. Res. Lett.*, *24*(11), 1315–1318.

Titov, V. V., and C. E. Synolakis (1998), Numerical modeling of tidal wave runup, *J. Waterw. Port Coast. Ocean Eng.*, *124*(4), 157–171.

Titov, V. V., H. O. Mofjeld, F. I. González, and J. C. Newman (1999), Offshore forecasting of Hawaiian tsunamis generated in Alaskan-Aleutian subduction zone, Pacific Marine Environmental Laboratory (PMEL), *NOAA Tech. Memo. ERL PMEL-114*, 26 pp.

Titov, V. V., F. I. González, E. N. Bernard, M. C. Eble, H. O. Mofjeld, J. C. Newman, and A. J. Venturato (2005), Real-time tsunami forecasting: Challenges and solutions, in *Developing Tsunami-Resilient Communities*, edited by E. Bernard, The National Tsunami Hazard Mitigation Program, *Nat. Hazards*, *35*(1), 40–58.

Tsunami Pilot Study Working Group (TPSWG) (2006), Seaside, Oregon Tsunami Pilot Study-Modernization of FEMA Flood Hazard Maps, *NOAA OAR Special Rep., NOAA/OAR/PMEL*, Seattle, WA, 94 pp. +7 appendices.

United Nations Development Programme (UNDP) Bureau for Crisis Prevention and Recovery (2004), *Reducing Disaster Risk: A Challenge for Development, A Global Report*, edited by M. Pelling et al., p. 146, John S. Swift Co.

Walsh, T. J., C. G. Caruthers, A. C. Heinitz, E. P. Myers III, A. M. Baptista, G. B. Erdakos, and R. A. Kamphaus (2000), Geologic Map GM-49: Tsunami Hazard Map of the Southern Washington Coast–Modeled Tsunami Inundation from a Cascadia Subduction Zone Earthquake, Washington State Department of Natural Resources Division of Geology and Earth Resources. (Available at http://www.dnr.wa.gov/)

Ward, S. N. (1994), A multidisciplinary approach to seismic hazard in southern California, *Bull. Seismol. Soc. Am.*, *84*, 1293–1309.

Wei, Y., E. N. Bernard, L. Tang, R. Weiss, V. V. Titov, C. Moore, M. Spillane, M. Hopkins, and U. Kânoğlu (2008), Real-time experimental forecast of the Peruvian tsunami of August 2007 for U.S. coastlines, *Geophys. Res. Lett.*, *35*, L04609, doi:10.1029/2007GL032250.

Wesson, R. L., A. D. Frankel, C. S. Mueller, and S. C. Harmsen (1999), Probabilistic Seismic Hazard Maps of Alaska, *U.S. Geological Survey, Open-File Rep. 99-36*, 20 pp.

Wesson, R. L., O. S. Boyd, C. S. Mueller, C. G. Bufe, A. D. Frankel, and M. D. Petersen (2007), Revision of time-Independent probabilistic seismic hazard maps for Alaska, *U.S. Geological Survey Open-File Rep. 2007-1043*, 38 pp.

Wong, F. L., A. J. Venturato, and E. L. Geist (2006), Seaside, Oregon, tsunami pilot study—Modernization of FEMA flood hazard maps: GIS Data: U.S. Geological Survey Data 236. (Available at http://pubs.usgs.gov/ds/2006/236/)

World Meteorological Organization (WMO) (2008), Urban Flood Risk Management—A Tool for Integrated Flood Management, Associated Programme on Flood Management Document 11, in Flood Management Tools Series, 38 pp. (Available at http://www.apfm.info/ifm_tools.htm)

Yeh, H., V. V. Titov, V. Gusyiakov, E. Pelinovsky, V. Khramushin, and V. Kaistrenko (1995), The 1994 Shikotan earthquake tsunami, *Pure Appl. Geophys.*, *144*(3/4), 569–593.

D. Arcas and J. Newman, Joint Institute for the Study of Atmosphere and Ocean, University of Washington, 3737 Brooklyn Avenue NE, Box 355672, Seattle, WA 98105-5672, USA.

D. Bellomo, Department of Homeland Security, FEMA, 500 C Street SW, Washington, DC, 20472, USA.

D. Carlton, ESA Adolfson, 5309 Shilshole Avenue NW #200, Seattle, WA 98107-5344, USA.

E. L. Geist, T. Parsons, and F. Wong, U.S. Geological Survey, MS-999, 345 Middlefield Road, Menlo Park, CA 94025, USA.

F. I. González, Department of Earth and Space Sciences, University of Washington, Johnson Hall Room-070, Box 351310, 4000 15th Avenue NE, Seattle, WA 98195-1310, USA. (figonzal@u.washington.edu)

T. Horning, Horning Geoscience, 2609 N Roosevelt Drive, Seaside, OR 97138, USA.

B. Jaffe, U.S. Geological Survey, Pacific Science Center, 400 Natural Bridges Drive, Santa Cruz, CA 95060, USA.

J. Johnson, Northwest Hydraulics Consultants, 16300 Christensen Road, Suite 350, Seattle, WA 98188-3422, USA.

U. Kânoğlu, Department of Engineering Sciences, Middle East Technical University, 06531 Ankara, Turkey.

H. Mofjeld, School of Oceanography, University of Washington, Box 357940, Seattle, WA 98195-7940, USA.

R. Peters, Robert Peters Geologic, P.O. Box 95, Davenport, CA 95017, USA.

C. Peterson, Geology Department, Portland State University, 17 Cramer Hall, 1721 SW Broadway, Portland, OR 97207-0751, USA.

G. Priest, Oregon Department of Geology and Mineral Industries, Coastal Field Office, 313 SW 2nd, Suite D, Newport, OR 97365, USA.

C. E. Synolakis, Viterbi School of Engineering, University of Southern California, 3650 McClintock Avenue, Los Angeles, CA 90089-2531, USA.

V. V. Titov, NOAA Pacific Marine Environmental Laboratory, 7600 Sand Point Way, NE, Seattle, WA 98115, USA. (vasily.titov@noaa.gov)

A. Venturato, Pierce County GIS Division, 615 So. 9th Street, Suite 300, Tacoma, WA 98405-4666, USA.

J. Weber, Department of Homeland Security, FEMA Region X, Federal Regional Center, 130 228th Street SW, Bothell, WA 98021-9796, USA.

A. Yalciner, Department of Civil Engineering, Middle East Technical University, 06531 Ankara, Turkey.